

Paleomagnetic evidence for a partially differentiated ordinary chondrite parent asteroid

J. F. J. Bryson^{1,2}, B. P. Weiss², B. Getzin³, J. N. H. Abrahams^{4,5}, F. Nimmo⁵,
A. Scholl⁶

¹Department of Earth, Atmospheric and Planetary Sciences, Massachusetts Institute of Technology, 77
Massachusetts Avenue, MA, 02139, USA

²Department of Earth Sciences, University of Cambridge, Downing Street, Cambridge, CB23EQ, UK

³Smith College, Northampton, MA, 01063, USA

⁴Division of Geological and Planetary Sciences, California Institute of Technology, Pasadena, CA, 91125,
USA

⁵Department of Earth and Planetary Sciences, University of California, Santa Cruz, CA, 95064, USA

⁶Advanced Light Source, Lawrence Berkeley National Laboratory, Berkeley, CA, 94720, USA

Key Points:

- The Portales Valley H6 chondrite experienced a magnetic field with properties consistent with dynamo fields at ~ 100 Myr after CAI formation.
- This observation indicates that the H chondrite parent body contained an advecting metallic core, so was partially differentiated.
- We model the thermal evolution of such bodies, finding they can reproduce the measured ages and cooling rates of multiple H chondrites.

Corresponding author: J. F. J. Bryson, jfjb2@cam.ac.uk

20 **Abstract**

21 The textures and accretion ages of chondrites have been used to argue that their par-
 22 ent asteroids never differentiated. Without a core, undifferentiated planetesimals could
 23 not have generated magnetic fields through dynamo activity, so chondrites are not ex-
 24 pected to have experienced such fields. However, the magnetic remanence carried by the
 25 CV chondrites is consistent with dynamo-generated fields, hinting that partially differ-
 26 entiated asteroids consisting of an unmelted crust atop a differentiated interior may ex-
 27 ist. Here, we test this hypothesis by applying synchrotron X-ray microscopy to metal-
 28 lic veins in the slowly-cooled H6 chondrite Portales Valley. The magnetic remanence car-
 29 ried by nanostructures in these veins indicates this meteorite recorded a magnetic field
 30 over a period of tens to hundreds of years at ~ 100 Myr after solar system formation. These
 31 properties are inconsistent with external field sources such as the nebula, solar wind, or
 32 impacts, but are consistent with dynamo-generated fields, indicating that the H chon-
 33 drite parent body contained an advecting metallic core and was therefore partially dif-
 34 ferentiated. We calculate the thermal evolution of the chondritic portions of partially
 35 differentiated asteroids that form through incremental accretion across $10^5 - 10^6$ years,
 36 finding this can agree with the measured ages and cooling rates of multiple H chondrites.
 37 We also predict the cores of these bodies could have been partially liquid and feasibly
 38 generating a dynamo at 100 Myr after solar system formation. These observations con-
 39 tribute to a growing body of evidence supporting a spectrum of internal differentiation
 40 within some asteroids with primitive surfaces.

41 **Plain language summary**

42 Asteroids formed during the first few million years of the solar system through the
 43 accretion of billions of mm-sized solids. If this process occurred within the first ~ 2 Myr
 44 of the solar system, the asteroid is thought to have partially melted, while if it occurred
 45 after this time, the asteroid is thought to have remained completely unmelted. Partial
 46 melting is an easy mechanism of an asteroid differentiating into a rocky mantle and metal-
 47 lic core. Recently, this discrete nature of asteroid melting has been challenged by mag-
 48 netic measurements of a group of unmelted meteorites that suggest they experienced mag-
 49 netic fields generated in an asteroid core, hinting that their parent asteroid contained
 50 melted and unmelted material and was therefore partially differentiated. Here, we show
 51 that a previously unmeasured type of unmelted meteorite recorded a magnetic field over

a period of tens to hundreds of years at ~ 100 million years after solar system formation. These timings make this a particularly robust observation that some unmelted meteorites experienced dynamo fields and originate from partially differentiated asteroids. This observation favours the episodic formation of some asteroids, potentially impacts our understanding of the thermal and structural history of the first planetary bodies in our solar system.

1 Introduction

Meteorites are classified into two primary petrographic types: chondrites, which are aggregates of nebular materials that remained unmelted on their parent planetesimals, and achondrites, which are the products of planetesimal melting processes (Weiss & Elkins-Tanton, 2013). A planetesimal’s thermal history and lithology depend predominantly on the time that it accreted. This parameter controls the concentration of short-lived radionuclides (principally ^{26}Al , which has a half-life of ~ 0.7 Myr) incorporated into the body and hence the amount of radiogenic heating it experiences. Thermal evolution models assuming instantaneous accretion predict that early-accreted bodies ($\lesssim 2$ Myr after the formation of calcium-aluminium-rich inclusions [CAIs]) partially melted and differentiated into a rocky mantle and metallic core, whereas bodies that accreted even slightly later ($\gtrsim 2$ Myr after CAI formation) remained unmelted and entirely undifferentiated (Hevey & Sanders, 2006). Combined with the common central assumption that groups of meteorites with similar chemical and isotopic signatures are samples of separate bodies, this predicted bimodality in planetesimal differentiation motivated the paradigm that chondrite and achondrite groups originate from distinct undifferentiated and differentiated bodies, respectively (Weiss & Elkins-Tanton, 2013).

Recently, the discrete nature of asteroid differentiation has been challenged by paleomagnetic measurements of CV chondrites, which argue that the post-accretional unidirectional natural remanent magnetisation (NRM) carried by these meteorites is the product of magnetic fields generated by core dynamo activity (Carpurzen et al., 2011; Fu et al., 2014; Gattacceca et al., 2016; Shah et al., 2017). This observation implies that the parent bodies of some chondrites were partially differentiated, consisting of a variably metamorphosed, but unmelted, chondritic crust atop a melted interior that contains an advecting metallic core (Elkins-Tanton et al., 2011). Thermal evolution models suggest that such partially differentiated bodies likely began forming when ^{26}Al was abun-

84 dant (i.e., $\lesssim 2$ Myr after CAI formation) and continued to accrete material (possibly episod-
 85 ically) for perhaps 0.5 - 4 Myr. These models also suggest these bodies could have gen-
 86 erated early (within the first $\sim 5 - 15$ Myr after CAI formation) magnetic fields (Elkins-
 87 Tanton et al., 2011; Bryson et al., 2019). However, the multi-stage and relatively poorly
 88 constrained thermal and aqueous alteration histories of CV chondrites as well as the an-
 89 tiquity of their NRM (likely recorded within 10 Myr of CAI formation, not long after
 90 nebula dissipation; Weiss and Elkins-Tanton (2013)) have motivated alternative hypothe-
 91 ses for the origin of their NRM other than core dynamo activity. These hypotheses in-
 92 clude the early solar wind (Tarduno et al. (2017), although see Oran et al. (2018)), the
 93 solar nebula (Cisowski, 1987) and/or transient impact-produced plasmas (Muxworthy
 94 et al., 2017).

95 A robust test of the hypothesis that some chondrites could have been magnetised
 96 by dynamo fields and that their parent bodies could have been partially differentiated
 97 would be to identify a stable NRM in a chondrite that underwent well-constrained and
 98 prolonged cooling over tens to hundreds of millions of years. This chondrite would have
 99 recorded its NRM long after nebula dissipation (only existed within the first $< 3.8 - 4.8$
 100 Myr; Wang et al. (2017)), cooled slowly enough that quick variations in the solar wind
 101 field (timescale of days) produce a very weak time-averaged intensity (< 3.5 nT; Oran
 102 et al. (2018)) and cooled negligibly within the extremely brief lifetime of impact gener-
 103 ated fields on asteroid-sized bodies (< 10 s; Crawford and Schultz (2000)). Compared to
 104 the CV chondrites, it is considerably less likely that this slowly cooled chondrite could
 105 have been magnetised by an external field. Instead, this chondrite is much more likely
 106 to have been magnetised by core dynamo fields, which are predicted to have been gen-
 107 erated tens to hundreds of Myr after CAI formation and for periods of possibly tens of
 108 Myr (Bryson et al., 2015; Nimmo, 2009). Hence, the observation of a young and long-
 109 lived remanence in a chondrite would provide robust evidence that its parent asteroid
 110 contained a core and was therefore partially differentiated. With this motivation, we present
 111 paleomagnetic measurements of the relatively young (the measured ^{40}Ar - ^{39}Ar ages of
 112 two Portales Valley samples are 90 ± 11 and 109 ± 14 Myr after CAI formation, which
 113 corresponds to the time the meteorite cooled through ~ 330 and ~ 230 °C, respectively;
 114 Bogard and Garrison (2009)) and slowly-cooled (metallographic cooling rate of 25 °C/Myr
 115 at ~ 500 °C; Scott et al. (2014)) H6 ordinary chondrite metal-silicate breccia Portales
 116 Valley (Ruzicka et al., 2005). This meteorite contains annealed microstructural evidence

117 that it experienced an early impact when it was at a temperature $>800 - 1000$ °C (Ruzicka
118 et al., 2015; Rubin, 2004), after which it remained essentially unshocked (did not expe-
119 rience shock pressures >5 GPa) during subsequent slow cooling (Scott et al., 2014; Stöfler
120 et al., 1991). Portales Valley was therefore above the Curie temperature of any magnetic
121 phases found in this meteorite (Rochette et al., 2003, 2008) when it last experienced a
122 significant impact, further ruling out the possibility that any stable NRM in Portales Val-
123 ley is the produce of an impact-generated field. Portales Valley therefore provides us with
124 an opportunity to examine the possibility that some chondrites were magnetised by late-
125 stage magnetic fields and that some chondrite parent bodies were partially differentiated.

126 Although ordinary chondrites make up $\sim 75\%$ of meteorites, they have largely evaded
127 reliable paleomagnetic study until now because their magnetic mineralogy is dominated
128 by magnetically-unstable multidomain grains and/or strongly magnetostatically-interacting
129 assemblages (Gattacceca et al., 2014). Portales Valley is unique among ordinary chon-
130 drites as it is composed of approximately equal portions of partially melted silicates and
131 cm-sized Fe-Ni veins. These metal veins contain microstructures that formed during low-
132 temperature recrystallisation upon slow cooling (Scott et al., 2014). One component of
133 these microstructures is the cloudy zone (CZ), a nano-scale intergrowth of islands of tetrataen-
134 ite (tetragonal, chemically ordered $\text{Fe}_{0.5}\text{Ni}_{0.5}$) and an Fe-rich matrix phase (Uehara et
135 al., 2011). Tetrataenite is an extremely magnetically hard mineral (intrinsic coercivity
136 >1 T) whose [001] magnetic easy axis forms along one of the three [100] axes of the par-
137 ent taenite phase (Néel et al., 1964). The presence of a magnetic field during tetrataen-
138 ite ordering has been proposed to have imparted a remanence to the CZ by influencing
139 the proportions of each of the [100] axes of the parent taenite that become the [001] mag-
140 netic easy axis of the tetrataenite (Bryson, Church, et al., 2014). The magnetisation of
141 the CZ can be studied in isolation from the bulk magnetisation of a metal-rich meteorite
142 using X-ray photoemission electron microscopy (XPEEM; Bryson, Herrero-Albillos, et
143 al. (2014)). This technique provides images of the CZ magnetisation from which the dis-
144 tribution of the easy axes among the tetrataenite islands and the properties of a mag-
145 netic field experienced by metal-rich meteorites can be estimated. XPEEM has previ-
146 ously been used to constrain the magnetic history of the main-group pallasites (Bryson
147 et al., 2015; Nichols et al., 2016) and the IVA (Bryson et al., 2017), IAB (Nichols et al.,
148 2016) and IIE (Maurel et al., 2018) iron meteorites.

149 Here, we apply XPEEM to the metal veins in Portales Valley with the aim of iden-
150 tifying whether this meteorite experienced a magnetic field when the tetrataenite islands
151 in its CZ chemically ordered and using our observations to constrain the differentiated
152 state of its parent body. We complement these measurements with a suite of asteroid
153 thermal evolution models aimed at identifying whether the thermal evolution of partially
154 differentiated bodies are consistent with measured thermal history of multiple H chon-
155 drites and the generation of a late-stage planetary magnetic field through dynamo ac-
156 tivity.

157 **2 Materials and Methods**

158 **2.1 General petrographic description**

159 Portales Valley is a unique chondrite that consists of partially melted silicates and
160 cm-sized Fe-Ni veins. Both of these components bear strong elemental and isotopic sim-
161 ilarities to the H chondrites, indicating that the protolith of Portales Valley was H chon-
162 drite material (Ruzicka et al., 2005). However, Portales Valley differs from other H chon-
163 drites because it reached higher peak metamorphic temperatures (940 - 1150 °C; Ruzicka
164 et al. (2005)). Portales Valley contains annealed evidence of an early shock event (likely
165 S3 - S6; Rubin (2004)) that occurred when the meteorite was at high temperature (>800
166 - 1000 °C; Ruzicka et al. (2015)). This observation led Ruzicka et al. (2005) to propose
167 that the metal veins in this meteorite could have formed when stresses from this impact
168 separated molten metal from partially molten silicates. There is no requirement from geo-
169 chemical observations for the addition of a significant amount of heat to the meteorite
170 during this impact, meaning that it is possible that the partial melting of Portales Val-
171 ley could have been the result of endogenic heat from ^{26}Al decay (Ruzicka et al., 2005).
172 If so, the petrography of Portales Valley would be evidence for the partial differentia-
173 tion of its parent body. However, it is also possible that this impact added some heat
174 to this meteorite, which, on top of the endogenic heat, could have caused its partial melt-
175 ing.

176 **2.2 Magnetic mineralogy**

177 A series of microstructures form in meteoritic metal during slow cooling. These mi-
178 crostructures start forming on cooling through ~ 900 °C when lamellae of the Ni-poor

179 phase kamacite nucleate and grow out of the parent taenite phase. Ni is rejected from
 180 these lamellae as they grow, introducing a Ni gradient in the adjacent taenite that varies
 181 from $\sim 50\%$ Ni immediately adjacent to the kamacite lamellae down to the bulk metal
 182 Ni concentration ($\sim 7\%$ Ni in Portales Valley; Ruzicka et al. (2005)) over 10 - 20 μm (Uehara
 183 et al., 2011). The gradient of this Ni zoning indicates that Portales Valley cooled at 25
 184 $^{\circ}\text{C}/\text{Myr}$ through ~ 500 $^{\circ}\text{C}$ (Scott et al., 2014).

185 On cooling below 320 $^{\circ}\text{C}$, pure tetrataenite forms as a rim adjacent to the kamacite
 186 lamellae at Ni compositions between $\sim 50 - 42\%$ (Goldstein et al., 2009). This rim forms
 187 from the same parent taenite as that of the CZ and contains large (>1 μm) twin domains,
 188 each consisting of one of the three different possible tetrataenite easy axes (Bryson, Herrero-
 189 Albillos, et al., 2014). The CZ forms adjacent to the rim at Ni concentrations between
 190 $\sim 42 - <25\%$ via spinodal decomposition (Maurel et al., 2019). This process starts at ~ 400
 191 $^{\circ}\text{C}$ and decreases in temperature as the Ni concentration decreases (Uehara et al., 2011).
 192 The islands that form at higher Ni concentration (those closer to the rim) therefore formed
 193 at higher temperatures and earlier times than those that formed at lower Ni concentra-
 194 tion (those further from the rim). This Ni concentration gradient also leads to a decrease
 195 in island size across the width of the CZ (Maurel et al., 2019). The similarity in the di-
 196 ameter of the largest islands in the CZ in both the silicate-rich portion (109 ± 5.2 nm)
 197 and the metal veins (106.3 ± 7.1 nm) indicate that these two constituents cooled at a
 198 single rate at temperatures below ~ 400 $^{\circ}\text{C}$ (Scott et al., 2014). The weighted average
 199 diameter of the CZ islands in both constituents of the Portales Valley is 108 nm (Scott
 200 et al., 2014).

201 Islands that form at temperatures between 400 - 320 $^{\circ}\text{C}$ do so as taenite and or-
 202 der to form tetrataenite as the meteorite cools through 320 $^{\circ}\text{C}$ (Einsle et al., 2018). Re-
 203 cent micromagnetic modelling (Einsle et al., 2018) demonstrates these islands recorded
 204 a new chemical transformation remanent magnetisation (CTRM) during ordering and
 205 that this remanence is independent of the magnetic state of the parent taenite. Conse-
 206 quently, all the islands that had formed before a meteorite reached 320 $^{\circ}\text{C}$ will have recorded
 207 a new remanence during ordering at the same time. The remanence across the width of
 208 the CZ is therefore unlikely to reflect a time-resolved record of dynamo activity over mil-
 209 lions of years as previously thought (Bryson et al., 2015; Nichols et al., 2016, 2018). Prior
 210 to this transition, these larger islands adopted vortex domain states, meaning they ex-
 211perienced relatively weak magnetostatic interaction fields (Einsle et al., 2018). Finer is-

212 lands that formed at temperatures <320 °C likely did so as single-domain tetrataenite,
 213 causing them to experience more intense interaction fields that possibly strongly favoured
 214 one easy axis among these islands (Bryson, Church, et al., 2014; Einsle et al., 2018). We
 215 intentionally do not analyse these fine islands due to these intense interactions. The tetrataen-
 216 ite ordering temperature is similar to the ^{40}Ar - ^{39}Ar closure temperature of Portales Val-
 217 ley ($\sim 330 - 230$ °C, Bogard and Garrison (2009)), indicating that the CZ in this mete-
 218 orite recorded its NRM ~ 100 Myr after CAI formation. The measured rate of tetrataen-
 219 ite disordering at 320 °C is certainly $\gg 11$ days and probably $\sim 30 - 300$ years (Dos San-
 220 tos et al., 2015). These disordering timescales indicate that tetrataenite ordering lasted
 221 for at least this period and was possibly longer as the rate of change in order parame-
 222 ter in binary alloys is often slower during ordering than disordering (e.g., Morris et al.
 223 (1974)). Remanence acquisition therefore occurred over a long time period relative to
 224 the duration of impact-generated fields (Crawford & Schultz, 2000) and the rate of change
 225 of the solar wind field (Oran et al., 2018).

226 The volume of the islands at the time that they ordered has been suggested to have
 227 played a significant role in the proportions of each of the possible easy axes that form
 228 among the CZ for a given field intensity (Bryson, Church, et al., 2014; Berndt et al., 2016).
 229 Through modelling spinodal decomposition, Maurel et al. (2019) found that islands had
 230 a radius of $\sim 78\%$ of their present day value when the CZ cooled through 320 °C for bulk
 231 CZ Ni concentrations of $\sim 40\%$. This value is far larger than the thermal blocking vol-
 232 ume of tetrataenite (which corresponds to a radius of 4 nm), greatly reducing the num-
 233 ber of islands required for estimates of the paleofield properties at 95% confidence from
 234 previous estimates of $\sim 100,000$ (Berndt et al. (2016), see Section 4.1). We present pa-
 235 leofield properties using an island volume corresponding to a radius of 42 nm (78% of
 236 the weighted average present-day radius of the largest islands). The island size decreases
 237 across the CZ, however the rate at which this occurs in our specific sample depends on
 238 the relative orientations of the surface we imaged and the kamacite lamellae. Regard-
 239 less, our adopted radius is likely an overestimate of the average island size across the re-
 240 gions we analysed, meaning that our paleointensity estimates are lower limits.

241 **2.3 X-ray photoelectron emission microscopy**

242 We obtained a sample of Portales Valley from the Natural History Museum, Lon-
 243 don (sample number BM 1999,M.50) that contained both the silicate- and metal-rich por-

244 tions of this meteorite. We captured XPEEM images at multiple locations along two sep-
 245 arate CZ-bearing interfaces (termed interface A and B, separated by ~ 6 mm, Fig. 1) at
 246 beamline 11.0.1 at the Advanced Light Source, Lawrence Berkeley National Laboratory.
 247 We imaged interface A in August 2015 during "two-bunch" synchrotron operation and
 248 interface B in February 2016 during normal synchrotron operation. Prior to XPEEM mea-
 249 surements, we sputtered our subsample with Ar ions (8 hours at 1.2 keV, followed by
 250 8 hours at 0.8 keV, and finally one hour at 0.6 keV) under ultra-high vacuum at the beam-
 251 line to ensure the surface was clean and to remove an ~ 80 nm thick magnetically soft
 252 layer that was introduced during polishing (Bryson, Church, et al., 2014; Bryson, Herrero-
 253 Albillos, et al., 2014).

254 The magnetic contrast in our XPEEM images is provided by X-ray magnetic cir-
 255 cular dichroism (XMCD), whereby the efficiency of electron ejection from the sample's
 256 surface by circularly polarised X-rays depends on the relative orientation of the local mag-
 257 netic moment and the X-ray beam (Bryson, Herrero-Albillos, et al., 2014). Once ejected
 258 from the sample surface, the electrons pass through a series of focusing lenses to gen-
 259 erate a map of the local projection of the surface magnetic moment onto the X-ray beam
 260 direction. This technique probes the magnetisation of the top ~ 5 nm of the sample. The
 261 XPEEM intensity, I , is calculated as the difference between images captured with right,
 262 I_R , and left, I_L , circular polarised X-rays, divided by the sum of these images:

$$I = \frac{I_R - I_L}{I_R + I_L} \quad (1)$$

263 We present I rather than I_R or I_L because I is independent of the sample's composi-
 264 tion and minimises effects of fluctuations in beam intensity. Blue and red signals in our
 265 XPEEM images correspond to positive and negative projections of the local magnetic
 266 moment onto the X-ray beam direction, respectively. We adopted a new experimental
 267 procedure during both beamtimes where we imaged each location at three orientations
 268 of the sample with respect to the X-ray beam. This methodology allowed us for the first
 269 time to directly estimate the direction and intensity of the ancient field experienced by
 270 the CZ, improving upon single field component and paleointensity lower limits presented
 271 in previous studies that imaged samples at only one sample orientation with respect to
 272 the X-ray beam (Bryson et al., 2015; Nichols et al., 2016; Bryson et al., 2017; Nichols
 273 et al., 2018). We achieved this by rotating the sample by $\sim 120^\circ$ around an axis perpen-
 274 dicular to its surface between measurements. Assuming the average proportion of each
 275 easy axis across a large number of CZ islands is dominated by the energy of that direc-

276 tion in a magnetic field with a given orientation and thermal fluctuations, the XMCD
 277 signal averaged over a region of the CZ, I_A , can be expressed as:

$$I_A = \frac{I_x e^{\frac{M_s V B_x}{k_B T_0}} + I_{-x} e^{-\frac{M_s V B_x}{k_B T_0}} + I_y e^{\frac{M_s V B_y}{k_B T_0}} + I_{-y} e^{-\frac{M_s V B_y}{k_B T_0}} + I_z e^{\frac{M_s V B_z}{k_B T_0}} + I_{-z} e^{-\frac{M_s V B_z}{k_B T_0}}}{e^{\frac{M_s V B_x}{k_B T_0}} + e^{-\frac{M_s V B_x}{k_B T_0}} + e^{\frac{M_s V B_y}{k_B T_0}} + e^{-\frac{M_s V B_y}{k_B T_0}} + e^{\frac{M_s V B_z}{k_B T_0}} + e^{-\frac{M_s V B_z}{k_B T_0}}} \quad (2)$$

278 where x , y and z are the three possible tetraenaite easy axes; I_x , I_{-x} , I_y , I_{-y} , I_z and
 279 I_{-z} are the XMCD intensities of the three pairs of possible tetraenaite magnetisation
 280 directions extracted from the tetraenaite rim corresponding to the easy axes; B_x , B_y
 281 and B_z are the components of the paleofield intensity along the easy axes; T_0 is the tetraenaite
 282 ordering temperature (320 °C); V is the mean volume of an island at T_0 ; M_s is the
 283 saturation magnetisation of tetraenaite at T_0 (1.12×10^6 A m⁻¹); and k_B is Boltzmann's
 284 constant (Bryson, Church, et al., 2014). This expression assumes that islands are mag-
 285 netically non-interacting; the errors and uncertainties introduced by this assumption are
 286 discussed in Section 4.1. The domains in the tetraenaite rim are typically >1 μ m along
 287 their longest dimension and display uniform values of I_x , I_{-x} , I_y , I_{-y} , I_z and I_{-z} pro-
 288 viding a means of reliably extracting these values from our XPEEM images (Fig. S1).
 289 We extracted these values from as many images as possible (the tetraenaite rims in some
 290 locations did not contain all six of these values), from which we calculated an average
 291 value of each of these intensities and used these averages values to recover paleointen-
 292 sities. For typical values of V ($\sim 5 \times 10^{-21}$ - 5×10^{-24} m³) and B_x , B_y and B_z (~ 1 -
 293 100 μ T), I_A can be approximated as:

$$I_A \approx \frac{M_s V}{6k_B T_0} ((I_{-x} - I_x) B_x + (I_{-y} - I_y) B_y + (I_{-z} - I_z) B_z) + \frac{1}{6} (I_x + I_{-x} + I_y + I_{-y} + I_z + I_{-z}) \quad (3)$$

294 Rotating a sample about an axis perpendicular to the surface changes the orientation
 295 of the X-ray beam with respect to the tetraenaite easy axes such that the values of I_x ,
 296 I_{-x} , I_y , I_{-y} , I_z and I_{-z} all change, while the paleofield components B_x , B_y and B_z re-
 297 main constant by definition. In this second rotation, the value of the average XMCD in-
 298 tensity, I'_A , can be approximated as:

$$I'_A \approx \frac{M_s V}{6k_B T_0} ((I'_{-x} - I'_x) B_x + (I'_{-y} - I'_y) B_y + (I'_{-z} - I'_z) B_z) + \frac{1}{6} (I'_x + I'_{-x} + I'_y + I'_{-y} + I'_z + I'_{-z}) \quad (4)$$

299 where I'_x , I'_{-x} , I'_y , I'_{-y} , I'_z and I'_{-z} are the XMCD intensities extracted from the tetraenaite
 300 rim in this second rotation from the same domains as in the previous rotation. Fi-
 301 nally, for a third sample orientation, the third average XMCD intensity, I''_A , can be ap-

302 proximated as:

$$I_A'' \approx \frac{M_s V}{6k_B T_o} ((I_{-x}'' - I_x'') B_x + (I_{-y}'' - I_y'') B_y + (I_{-z}'' - I_z'') B_z) + \frac{1}{6} (I_x'' + I_{-x}'' + I_y'' + I_{-y}'' + I_z'' + I_{-z}'') \quad (5)$$

303 where I_x'' , I_{-x}'' , I_y'' , I_{-y}'' , I_z'' and I_{-z}'' are the XMCD intensities extracted from the tetraena-
 304 ite rim in this third rotation. We calculated B_x , B_y and B_z by solving equations (3), (4)
 305 and (5) simultaneously using I_A , I_A' , I_A'' values extracted from one large region ($\sim 9 \mu\text{m}$
 306 $\times \sim 2 \mu\text{m}$) in the CZ starting adjacent to the tetraenaite rim at each of our locations
 307 (Fig. 2). We analysed regions of this size to incorporate as many islands as possible that
 308 do not display an XMCD signal indicating that their remanence has clearly been influ-
 309 enced by interactions that favour one easy axis. Furthermore, as discussed in Section 4.1,
 310 magnetostatic interactions likely influenced the CZ remanence, so analysing wide regions
 311 of the CZ that contain islands further from the rim that are separated by relatively large
 312 distances compared to their size likely reduces the impact of these interactions on our
 313 recovered paleofield properties.

314 We assessed the quality of all of the images we captured and disregarded any that
 315 contained detrimental beam drift or sample tilting that defocused or introduced a back-
 316 ground intensity ramp to the images. We accepted 18 of the locations we imaged along
 317 interface A and 19 locations along interface B.

318 As mentioned earlier, the rate of island size decrease across the CZ along the in-
 319 terfaces we measured depends on the orientation of our sample surface and the kamacite
 320 lamellae. If the lamellae and surface are nearly parallel, the island size is essentially con-
 321 stant across the width of the CZ we analysed. On the other hand, if the lamellae and
 322 surface are perpendicular, previous studies (Uehara et al., 2011; Bryson, Church, et al.,
 323 2014; Einsle et al., 2018) suggest that islands at a distance of $\sim 2 \mu\text{m}$ from the tetraena-
 324 ite rim are ~ 0.5 times the size of those next to the rim (i.e., radius of 21 nm when they
 325 recorded a remanence in Portales Valley). Assuming that the island radius is 42 nm across
 326 the width of the CZ that we analysed and that the islands occupy 90% of the CZ (Maurel
 327 et al., 2019) provides an estimate on the lower limit of the number of islands we imaged
 328 along each interface of $\sim 47,000$. Assuming an island radius of 21 nm across the width
 329 of the CZ provides an estimate on the upper limit of the number of islands we imaged
 330 along each interface of $\sim 190,000$ (see Section 4.1).

331 2.4 Asteroid thermal modelling

332 The thermal evolution of the H chondrite parent body has been constrained by a
 333 variety of thermochronometers and cooling rate measurements on multiple H chondrites.
 334 Asteroid thermal evolution models have demonstrated that undifferentiated but variably
 335 metamorphosed bodies are broadly compatible with these data (Henke et al., 2013; Mon-
 336 nereau et al., 2013), although the existence of an onion-shell thermal structure through-
 337 out the entire cooling history of the H chondrite parent body is debated (Scott et al.,
 338 2014; Blackburn et al., 2017). A key test of the hypothesis that the H chondrite body
 339 was partially differentiated is that the thermal evolution of such a body should be com-
 340patible with the available thermochronometry and cooling rate data. To assess whether
 341this could be the case, we performed 1-dimensional models of the thermal evolution of
 342a spherical body that accreted in two discrete events (Bryson et al., 2019). The math-
 343ematical description of our model and values of the parameters we adopted are detailed
 344by Bryson et al. (2019). We model the thermal evolution of a body that forms through
 345instantaneous accretion of material with thermal diffusivity $\kappa = 9 \times 10^{-7} \text{ m}^2 \text{ s}^{-1}$ (Opeil
 346et al., 2012) at time t_1 with radius r_1 that is covered at a later time, t_2 , by a large num-
 347ber of cold chondrules that increase its radius to r_2 (Elkins-Tanton et al., 2011). This
 348process has been proposed as a likely growth mechanism for asteroids with radii >100
 349km (Johansen et al., 2015). The initial body forms early enough that it can differenti-
 350ate and form a core, and the later addition of chondrules to its surface could result in
 351a partially differentiated body if some of these chondrules survive metamorphism with-
 352out melting. Our model is idealised and our intention is not to identify the exact prop-
 353erties, thermal evolution or accretional history of the H chondrite parent asteroid but
 354simply to assess the feasibility that the modelled thermal evolutions of partially differ-
 355entiated and undifferentiated bodies are similarly consistent with the measured thermal
 356evolutions measured of multiple H chondrites. If we demonstrate that our accretion sce-
 357narios are compatible with measured ages and cooling rates, partial differentiation should
 358be considered as one potential model for the H chondrite parent body given that there
 359are innumerable other possible gradual accretion scenarios with different accretion rates
 360and durations that might also produce these bodies (e.g., Lichtenberg et al. (2018)).

361 We conducted 2,000 simulations with randomly chosen combinations of r_1 , t_1 , r_2
 362 and t_2 . Values of t_1 were chosen at random from a uniform distribution spanning 0.0 -
 363 2.0 Myr after CAI formation, corresponding to the period when the accreting material

364 contained enough ^{26}Al to partially melt. Values of t_2 were chosen between 2.0 - 4.5 Myr
 365 after CAI formation, corresponding to the period when the material added in the sec-
 366 ond event was variably heated but not melted by ^{26}Al decay. Values of r_1 were chosen
 367 between 20 - 500 km and values of r_2 were chosen between $r_1 + 1$ and 500 km. These
 368 radii ranges incorporate the smallest bodies that could retain enough radiogenic heat to
 369 cause differentiation (Hevey & Sanders, 2006) and extend up to the size of the largest
 370 asteroids in the asteroid belt at the present day.

371 We judged the quality of each random parameter combination by comparing the
 372 thermal evolutions at depth throughout the added chondritic material to the measured
 373 ages of multiple H chondrites that have been dated using multiple geochronological sys-
 374 tems with different closure temperatures (Kleine et al., 2008; Blinova et al., 2007; Bou-
 375 vier et al., 2007; Amelin et al., 2005; Trieloff et al., 2003). We considered the ^{182}Hf - ^{182}W ,
 376 ^{207}Pb - ^{206}Pb in silicates, ^{207}Pb - ^{206}Pb in phosphates, ^{40}Ar - ^{39}Ar and ^{244}Pu -fission track
 377 ages measured from the Richardton, Kernouvé and Estacado H chondrites (Table S1 in
 378 the Supporting Information) and the ^{207}Pb - ^{206}Pb in phosphates, ^{40}Ar - ^{39}Ar and ^{244}Pu -
 379 fission track ages measured from Ste. Marguerite. We did not consider the ^{182}Hf - ^{182}W
 380 and ^{207}Pb - ^{206}Pb in silicates ages measured from Ste. Marguerite as it has previously been
 381 argued that the peak metamorphic temperature experienced by this meteorite was in-
 382 sufficient to reset these geochronological systems so they date chondrule formation rather
 383 than parent body metamorphism (Henke et al., 2013). Furthermore, we also considered
 384 the measured radiometric ages of the Forest Vale, Nadiabondi, Allegan, Mt. Browne and
 385 Guareña H chondrites (Table S1 in the Supporting Information). However, due to the
 386 sparsity and/or uncertainty in their ages, these meteorites do not additionally constrain
 387 the parent body properties or thermal evolution and consequently are only discussed fur-
 388 ther in the Supporting Information.

389 For a given parameter combination, the depth within the chondritic layer that pro-
 390 duced the thermal evolution that closest matched the closure temperatures at the mea-
 391 sured ages of a given meteorite is assigned as the depth of that meteorite. We calculated
 392 the closeness of the thermal evolution at each depth, C , as the sum of the square of the
 393 temperature difference between the model thermal evolutions, T_{calc} , and the closure tem-
 394 peratures, T_{ct} , at the measured ages for a given meteorite:

$$C = \Sigma[(T_{ct} - T_{calc})^2] \quad (6)$$

395 We present a total average residual value, R , calculated as the square root of the sum
 396 of the minimum closeness values, C_{min} , for all four meteorites divided by the total num-
 397 ber of measured ages, n , from all four meteorites:

$$R = \frac{\sqrt{\Sigma C_{min}}}{n} \quad (7)$$

398 This value is a measure of the overall fit quality for a given parameter combination, with
 399 lower values corresponding to better fits. The error bars on the data points correspond
 400 to 95% confidence on the ages and realistic estimates of the uncertainty in the closure
 401 temperatures (Kleine et al., 2008; Henke et al., 2013; Monnereau et al., 2013). These ranges
 402 create rectangular regions in age-closure temperature space through which acceptable
 403 simulated thermal evolutions of each meteorite would ideally pass. The total number of
 404 these rectangular regions from Ste. Marguerite, Richardton, Kernouvé and Estacado that
 405 are missed by their simulated thermal evolution curve is termed the score, S , with lower
 406 values corresponding to better fits to the measured thermal evolutions.

407 We also conducted thermal evolution models of undifferentiated bodies. These mod-
 408 els allowed us to compare the qualities of the fits recovered from our partially differen-
 409 tiated model directly with those recovered from equivalent models of undifferentiated bod-
 410 ies. The parameters and underlying mathematical description of the two models are iden-
 411 tical (Bryson et al., 2019). The undifferentiated models simply involved the production
 412 and conduction of radiogenic heat from ^{26}Al decay. We conducted 2,000 of these mod-
 413 els with random combinations of accretion time, t , ranging between 2.0 - 4.5 Myr after
 414 CAI formation and radius, r , ranging between 20 - 500 km. We calculated R and S val-
 415 ues for these models through the same method as the partially differentiated model and
 416 compared them with those calculated in the partially differentiated model.

417 **3 Results**

418 **3.1 X-ray photoemission electron microscopy**

419 Representative XPEEM images of the CZ along interface A and B at all three sam-
 420 ple rotations with respect to the X-ray beam are shown in Fig. 2. We extracted I_A , I'_A
 421 and I''_A values from one large region ($\sim 9 \times 2 \mu\text{m}$, grey boxes) of the CZ at all locations
 422 we analysed. The paleodirections we recover from these values are within error of each
 423 other along each interface accounting for the scatter in I_A , I'_A and I''_A values from loca-
 424 tion to location (Fig. 3a). The recovered paleointensities are $19 \pm 12 \mu\text{T}$ for interface

425 A and $9 \pm 7 \mu\text{T}$ for interface B (total 95% error) (Fig. 3b), also within error of each other.
 426 The errors and uncertainties on these values are discussed in Section 4.1. These values
 427 are lower limits given the likely decrease in island size across the CZ regions we analysed.

428 Although our recovered paleointensities are $>0 \mu\text{T}$ to 95% confidence, we made cer-
 429 tain that our measured remanences could not reflect the absence of a field by calculat-
 430 ing the range of paleointensities we would expect for equal probabilities that an island
 431 adopts any one of the six possible magnetisation directions (expected magnetisation con-
 432 figuration in the absence of a field) over 47,000 islands with a radius of 42 nm and 190,000
 433 islands with a radius of 21 nm (encompassing the range of island sizes and numbers that
 434 we possibly analysed). The mathematical details of this method are described by Bryson
 435 et al. (2017). We repeated this process 10,000 times, finding that 95% of these calcula-
 436 tions produce paleointensities $\leq 0.5 \mu\text{T}$ and $\leq 2.0 \mu\text{T}$ for 42 nm and 21 nm islands, re-
 437 spectively (Fig. 4). Regardless of the island size we adopt, our recovered paleointensi-
 438 ties are greater than these limits, allowing us to exclude with 95% confidence the pos-
 439 sibility that our XPEEM images correspond to the absence of a field.

440 The recovered paleodirections have 95% confidence ellipses of 11° and 37° along
 441 interfaces A and B, respectively, taking into account the measurement uncertainty (scat-
 442 ter in average XMCD values extracted from location to location along an interface). These
 443 values are shown in Fig. 3a as the 95% confidence ellipses. Our analysis procedure pro-
 444 vides the projection of the field direction along each of the three possible tetrataenite
 445 easy axis directions along a given interface. Interface A and B are located in separate
 446 grains (Fig. 1) with different crystallographic orientations, so we had to map the recov-
 447 ered directions onto the same directional framework to mutually orient our recovered di-
 448 rections and assess whether they are unidirectional. We accomplished this by first es-
 449 timating the directions of the three possible easy axes along each interface relative to the
 450 bounding box of the images from the values of the XMCD intensity of the domains in
 451 the tetrataenite rim at each sample rotation. We then generated the rotation matrix re-
 452 lating these axes and applied it to the directions recovered from the different CZ regions
 453 along each interface. The orientations we recovered from the XMCD intensities in the
 454 rim were not orthogonal (most likely because of slight moment relaxation), introducing
 455 an error in the recovered paleodirections (see Supporting Information). The 95% con-
 456 fidence error associated with this uncertainty is 16° and 34° along interfaces A and B,

457 respectively, which is similar to the 95% confidence angle calculated from the measure-
 458 ment uncertainty.

459 The paleodirections we recover are unidirectional and the paleointensities we re-
 460 cover are greater than zero, indicating that Portales Valley recorded a spatially-uniform
 461 field over a relatively long time period (likely tens to hundreds of years) at ~ 100 Myr
 462 after CAI formation.

463 3.2 Asteroid thermal modelling

464 A summary of the results of our partially differentiated asteroid thermal evolution
 465 models is shown in Fig. 5. Our models demonstrate that the late accretion of cold chon-
 466 drites to the surface of differentiated bodies can result in the addition of an undifferen-
 467 tiated layer on these bodies, producing partially differentiated bodies (Fig. 5b). We de-
 468 fined that a random parameter combination produced an acceptable fit to the measured
 469 ages if $R \leq 27$ °C, which corresponds to 95% of parameter combinations with $S \leq 6$
 470 (Fig. 5c). We find that wide ranges of r_1 , t_1 and r_2 are capable of producing acceptable
 471 fits to the measured H chondrite ages (Fig. 5a,d,e) and measured cooling rates (Fig. 6)
 472 of multiple H chondrites. The primary parameter that controls the values of R and S
 473 is t_2 , which produces acceptable values of these parameters between 2.3 - 2.5 Myr after
 474 CAI formation (Fig. 5d,e). The fit quality is also controlled to a lesser extent by the thick-
 475 ness of the added chondritic layer ($r_2 - r_1$). The relatively short duration of the period
 476 that produces acceptable fits stems from exponential changes in the amount of heat gen-
 477 erated by the decay of ^{26}Al associated with small changes in t_2 . Any difference in the
 478 values of t_2 that produce the best fits in our models and the accretion times recovered
 479 from previous models of undifferentiated bodies (Kleine et al., 2008; Henke et al., 2013;
 480 Monnereau et al., 2013; Doyle et al., 2015) originates from the different values of the ini-
 481 tial concentration of ^{26}Al in the chondritic material, the adopted heat capacity of the
 482 material in the models and the additional heat supplied to the chondritic layer from the
 483 initial body. We achieved our best fit ($R = 14.5$ °C, $S = 5$) for $r_1 = 65$ km, $t_1 = 0.6$ Myr
 484 after CAI formation, $r_2 = 178$ km and $t_2 = 2.45$ Myr after CAI formation (Fig. 5a). Our
 485 modelled cooling rates at 500 °C for the recovered depth of Richardton (19.7 °C/Myr),
 486 Kernouvé (7.3 °C/Myr) and Estacado (5.7 °C/Myr) are similar to measured values (20
 487 °C/Myr for Richardton and 10 °C/Myr for Kernouvé and Estacado), while our modelled
 488 cooling rate of Ste. Marguerite (46.9 °C/Myr) is significantly slower than the measured

489 cooling rate ($>10,000$ °C/Myr; Scott et al. (2014)). In fact, this measured rate is far quicker
 490 than that achieved in any of our models, indicating that it is likely due to a non-ideal
 491 process not included in our model (e.g., impacts) that could excavate material from depth
 492 and allow it to suddenly cool uncharacteristically quickly.

493 A summary of the results of our undifferentiated asteroid thermal models is shown
 494 in Fig. 7. We found that the parameters that produce acceptable fits in our partially dif-
 495 ferentiated model also produce acceptable fits in our undifferentiated model (Fig. 7a,b,c).
 496 Again, the quality of the fit depends primarily on the time of chondrule accretion and
 497 to a lesser extent the thickness of the chondritic layer (which in this model is the radius
 498 of the body). The modelled cooling rates are similar to those recovered from the parti-
 499 tially differentiated body (19.5 °C/Myr, 8.7 °C/Myr and 7.5 °C/Myr for Richardton,
 500 Kernové and Estacado, respectively; the recovered depth of Ste. Marguerite did not reach
 501 500 °C in this model). Our undifferentiated body produced marginally better fits (our
 502 best fit produces $R = 12.7$ °C and $S = 2$ for $r = 140$ km, $t = 2.47$ Myr after CAI for-
 503 mation) than our partially differentiated model due to the slightly prolonged cooling at
 504 later times in our partially differentiated bodies due to their larger size and the grad-
 505 ual conduction of heat from the interior of the body. In reality, it is possible that the later
 506 stages of the thermal evolution of a meteorite could have been effected by changes in cool-
 507 ing rates caused by processes not included in our model, such as regolith production and
 508 impacts (Warren, 2011). Importantly, the differences in R and S between our partially
 509 differentiated and undifferentiated models for similar values of t_2 and thickness of chon-
 510 dritic layers are very small compared to the variation in R and S for different param-
 511 eter combinations within either model. Furthermore, models of both types of body are
 512 capable of readily producing acceptable fits of equally good quality for a number of pa-
 513 rameter combinations. Therefore, the measured ages and cooling rates of multiple H chon-
 514 drites equally support an undifferentiated and partially differentiated H chondrite par-
 515 ent body.

516 The proportion of the chondritic portion of a body that remains unmelted in our
 517 partially differentiated models depends primarily on $r_2 - r_1$ and t_2 . Bodies with ear-
 518 lier t_2 values produce more radiogenic heat in their chondritic portions, so this material
 519 melts more readily when heat from the centre of the body passes into this material. It
 520 is likely that $>10\%$ of the radius of the added chondritic material survives metamorphism

521 without melting for $r_2 - r_1 \gtrsim 10$ km and $t_2 > 2.5$ Myr after CAI formation. This pro-
 522 portion increases as the thickness of the chondritic layer increases (Fig. 5b).

523 The relatively low internal pressures within asteroid-sized bodies have been pro-
 524 posed to have caused either outward or inward core solidification depending on the core's
 525 light element concentration (Williams, 2009). Outward core solidification creates a grav-
 526 itationally unstable density stratification in the core liquid that has been proposed to
 527 have been an efficient mechanism of dynamo generation within cores of asteroid-sized
 528 bodies (Nimmo, 2009; Bryson et al., 2019). Inward core solidification has been proposed
 529 to have generated dynamo activity through exotic, non-concentric solidification (Ruckriemen
 530 et al., 2015; Bryson et al., 2017; Neufeld et al., 2019). Although many of the details and
 531 timings of these processes are uncertain, it is clear that a core cannot generate a mag-
 532 netic field once it had solidified completely. The timing of the end of core solidification
 533 in our model depends primarily on the final radius of the body. Bryson et al. (2019) sug-
 534 gest that bodies with $r_2 > 170$ km and $2.0 < t_2 < 2.5$ Myr after CAI formation (pe-
 535 riod during which radiogenic abundances were high enough that the peak metamorphic
 536 temperatures of the H chondrites could be achieved through radiogenic heating) had at
 537 least partially molten cores at 100 Myr after CAI formation, so could feasibly have gen-
 538 erated magnetic fields when the CZ in Portales Valley recorded a remanence. Our mod-
 539 els of partially differentiated bodies with r_2 in this range are capable of producing ther-
 540 mal evolutions with acceptable fits to the measured H chondrite ages (Fig. 8). It is there-
 541 fore possible that partially differentiated bodies with a wide range of radii can explain
 542 the measured thermal evolution and remanent magnetisation of the H chondrites.

543 4 Discussion

544 4.1 Uncertainties in field properties recovered from the cloudy zone

545 Maurel et al. (2019) outline three sources of uncertainty in paleointensity and paleo-
 546 leodirection estimates recovered from XPEEM measurements of the CZ: 1) statistical
 547 uncertainty due to analysing a limited number of islands; 2) measurement uncertainty
 548 due to scatter in I_A , I'_A and I''_A from location to location (see Supporting Information);
 549 3) uncertainties in the bulk Ni concentration of the CZ that impacts the statistical un-
 550 certainty by effecting the size of islands when the meteorite cooled through 320 °C. Re-
 551 garding the statistical uncertainty, we analysed between 47,000 - 190,000 islands along

552 each interface depending on rate of decrease of island size across the CZ in our sample
 553 (see Section 2.3). According to the analysis of Maurel et al. (2019) and Berndt et al. (2016),
 554 and adopting an island radius of 78% of the islands at the present day at the time of tetrataen-
 555 ite ordering (Maurel et al., 2019) and a 14 μT field (the average lower limit recovered
 556 from the two interfaces we studied), these island numbers produce statistical uncertain-
 557 ties between 2 - 6%. The measurement uncertainty in our recovered paleointensities is
 558 63% (12 μT) and 78% (7 μT) for interface A and B, respectively. These values were cal-
 559 culated from the standard deviations in the paleointensities recovered from each loca-
 560 tion along each interface (Fig. S2 in the Supporting Information) and likely reflect vari-
 561 ations in the properties of the X-ray beam and the direction and intensity of magneto-
 562 static interaction fields from location to location. The Ni concentration is typically un-
 563 certain to $\pm 1\%$, which corresponds to a 15% uncertainty in paleointensity (Maurel et al.,
 564 2019). Together, these three uncertainties yield total maximum uncertainties of 65% (12
 565 μT) and 80% (7 μT) for interface A and B, respectively. These values are dominated by
 566 the measurement uncertainty. These total errors are inconsistent with a recovered pa-
 567 leointensity of 0 μT , so our data indicate that the CZ in Portales Valley experienced a
 568 field when its islands ordered to form tetrataenite. This conclusion is supported by the
 569 range of possible field intensities we calculate from simulated island magnetisation con-
 570 figurations expected in the absence of a field (Fig. 4).

571 Another potentially significant source of uncertainty not included in the approach
 572 outlined by Maurel et al. (2019) or Section 2.3 is island-island magnetostatic interactions.
 573 The proximity of the islands in the CZ means that fields emanating from one island could
 574 influence the magnetisation of neighbouring islands. This is almost certainly the case among
 575 the coarsest islands, which are separated by distances less than their size. If the under-
 576 lying CZ island magnetisation is random (expected configuration in the absence of an
 577 external field), this interaction field is also expected to be randomly oriented across the
 578 CZ. This field is therefore not expected to impart a uniform remanence across the CZ
 579 from location to location and certainly not from interface to interface. This prediction
 580 is verified by the results of Nichols et al. (2016, 2018), who recovered random island mag-
 581 netisation directions and very weak paleointensities (probably $< 1 \mu\text{T}$ and certainly within
 582 error of zero; Maurel et al. (2019)) from younger pallasites and IAB iron meteorites. This
 583 observation demonstrates that interactions between islands do not result in uniform re-
 584 manences across the CZ. In the presence of an external field, the field experienced by each

585 island across a meteorite is likely a combination of this uniform external field and the
586 local interaction field experienced by each island. In this scenario, it is possible that the
587 remanence carried by the CZ contains a uniform component imparted by the external
588 field. Importantly, the extent of the uniformity introduced by the external field could
589 be influenced and possibly reduced by the local interaction fields. A detailed micromag-
590 netic study of the role of interaction fields on CZ island magnetisation has yet to be con-
591 ducted, so their effect is not included in the paleointensity recovery approach detailed
592 in Section 2.3. Importantly, interactions could potentially represent a significant source
593 of uncertainty in our recovered paleointensities. If a future study quantifies the effect of
594 these interactions on the magnetisation of the CZ, we could use this result to recover more
595 reliable paleointensities from the data presented in the current study. Regardless of the
596 uncertainties associated with magnetostatic interactions, our observation of relatively
597 uniform paleodirections from location to location and interface to interface as well as our
598 recovered non-zero paleointensities are not expected in the absence of a field, indicat-
599 ing that the CZ in Portales Valley experienced a field when it chemically ordered. Cru-
600 cially, the key conclusions we draw regarding the partially differentiated state of the H
601 chondrite parent body rely only on Portales Valley having experienced an ancient field,
602 rather than the paleointensity of this field. Hence, the reliability of this conclusion is not
603 affected by uncertainties introduced by island-island magnetostatic interactions.

604 **4.2 Nature of the field that magnetised Portales Valley**

605 The unidirectional remanence we measured in Portales Valley indicates that this
606 meteorite recorded a relatively long-lived field (tens to hundreds of years) compared to
607 the lifetime of impact generated fields and the timescale of variations in the solar wind
608 field at ~ 100 Myr after CAI formation over a long period.

609 The small values of the average XMCD intensities extracted from the CZ along both
610 interfaces imply that the NRM is a small percentage of the saturation magnetisation,
611 indicating that the magnetisation of the CZ in our sample of Portales Valley has not been
612 overprinted by a hand magnet (see results of Gattacceca and Rochette (2004) for exam-
613 ples of strong remanences in overprinted meteorites). Furthermore, the coercivity of tetrataen-
614 ite in the CZ ranges from 0.2 - >2.0 T (Néel et al., 1964; Uehara et al., 2011; Bryson,
615 Church, et al., 2014), requiring direct exposure to a very strong rare Earth magnet to
616 alter its remanence. If our sample had been remagnetised by such a hand magnet, we

617 would expect to recover paleointensities in this range. These values are orders of mag-
 618 nitude more intense than the values we recover, further supporting the pristine nature
 619 of the NRM carried by our sample of Portales Valley.

620 It has been suggested previously that the remanence carried by other chondrites
 621 could have been imparted by fields generated by the nebula (Cisowski, 1987), the solar
 622 wind (Tarduno et al., 2017) or generated by impacts (Muxworthy et al., 2017). The young
 623 age of NRM acquisition in Portales Valley (~ 100 Myr after CAI formation; Bogard and
 624 Garrison (2009)) rules out direct magnetisation by the nebular field, which had dissipated
 625 by $< 3.8 - 4.8$ Myr after CAI formation (Gattacceca et al., 2016; Wang et al., 2017). The
 626 longevity of the recording period in Portales Valley (likely tens to hundreds of years) ex-
 627 cludes direct magnetisation by the solar wind field, which varies in orientation over a pe-
 628 riod of just a few days, resulting in a time-averaged intensity during the early solar sys-
 629 tem > 3 orders of magnitude weaker than our recovered paleointensities (Oran et al., 2018).
 630 Additionally, Nichols et al. (2016, 2018) recovered random magnetisation directions and
 631 very weak paleointensities from XPEEM measurements of young pallasites and the IAB
 632 iron meteorites. These meteorites experienced the solar wind field at a broadly similar
 633 time to Portales Valley, so this weak remanence demonstrates that the solar wind does
 634 not impart a recoverable remanence to the CZ. Prolonged remanence acquisition by the
 635 CZ also rules out transient fields generated by impacts, which are expected to last $\lesssim 10$
 636 s on asteroid-sized bodies (e.g., Crawford and Schultz (2000)). Furthermore, Portales Val-
 637 ley contains annealed microstructural evidence that it last experienced a significant im-
 638 pact (> 5 GPa) when it was $> 800 - 1000$ °C (Ruzicka et al., 2015), above the Curie tem-
 639 perature of any of the magnetic phases found in this meteorite (Rochette et al., 2003,
 640 2008). Therefore, Portales Valley was incapable of recording a remanence of any mag-
 641 netic fields it may have experienced immediately following this impact. Finally, the CZ
 642 islands recorded a new remanence as they ordered to form tetrataenite (Einsle et al., 2018),
 643 meaning that, even in the extremely unlikely and unexpected scenario that the parent
 644 taenite phase had somehow acquired a remanence, this remanence is not reflected in the
 645 magnetisation of the tetrataenite islands.

646 It is conceivable that a remanence imparted by an external field source to the early
 647 (first 5 - 10 Myr of the solar system) H chondrite crust could have generated a static re-
 648 manent field that subsequently imparted a remanence to the CZ in Portales Valley (see
 649 Fu et al. (2012), for an example of a meteorite that has been proposed to have been mag-

650 netised by such a field). To assess this possibility, we characterised the magnetisation
 651 of the H4 chondrite Forest Vale (summarised in Table S2 in the Supporting Information),
 652 which cooled sufficiently quickly (10,000 °C/Myr through ~500 °C) that it preserved the
 653 magnetic properties of the H chondrite crust from this early period (Scott et al., 2014;
 654 Gattacceca et al., 2014). Our alternating field (AF) demagnetisation measurements (Kirschvink,
 655 1980; Kirschvink et al., 2008; Tauxe & Staudigel, 2004; Stephenson, 1993; Weiss & Tikoo,
 656 2014), viscous relaxation measurements and stray field calculations demonstrate that this
 657 meteorite can only acquire a low coercivity anhysteretic remanent magnetisation (an ana-
 658 logue for thermoremanent magnetisation) that is weak, unstable and easily susceptible
 659 to pressure demagnetisation (Tikoo et al., 2015) (see Supporting Information). These
 660 observations indicate that it is extremely unlikely that the ancient H chondrite crust was
 661 capable of acquiring and preserving a crustal remanence and generating a strong and sta-
 662 ble remanent field when Portales Valley recorded its remanence, indicating that this phe-
 663 nomenon is not the source of the remanence in Portales Valley.

664 The longevity and age of the field we recover from Portales Valley are consistent
 665 with the expected properties of fields generated by dynamo activity (Weiss & Elkins-Tanton,
 666 2013; Weiss et al., 2010; Bryson et al., 2019). Coupled with the inconsistent properties
 667 of this field with potential external sources, this observation indicates that Portales Val-
 668 ley experienced a dynamo field. These fields are generated by the organised advection
 669 of molten metal in a planetary core, implying that the H chondrite parent body contained
 670 a metallic core. Combined with the unmelted nature of the H chondrites, this observa-
 671 tion indicates that the H chondrite parent body contained both unmelted material and
 672 material that partially melted and differentiated. This conclusion suggests that the H
 673 chondrite parent body was partially differentiated and consisted of an unmelted exte-
 674 rior atop a differentiated interior. Our asteroid thermal modelling demonstrates that such
 675 bodies could have formed through incremental accretion and that the thermal evolution
 676 of these bodies can be consistent with the measured ages (Fig. 5a,d,e) and cooling rates
 677 (Fig. 6) of multiple H chondrites. Additionally, these models demonstrate that the cores
 678 of these bodies could have been partially molten (i.e., feasibly capable of generating compositionally-
 679 driven dynamo fields) at the time Portales Valley recorded a remanence for final radii
 680 $\gtrsim 170$ km (Fig. 8). Together, the measured remanent magnetisation and thermal evo-
 681 lution of the H chondrite parent body are consistent with a partially differentiated par-
 682 ent asteroid, suggesting that such bodies formed during the early solar system.

683 Two other pieces of evidence exist that potentially support a partially differenti-
 684 ated H chondrite parent body. Firstly, the IIE iron meteorites contain silicate inclusions
 685 with geochemical and isotopic affinities to the H chondrites, indicating that these me-
 686 teorites originate from metal pools embedded in the mantle of an H chondrite-like body.
 687 The lithology of these inclusions range from unmelted and chondrule-bearing to com-
 688 pletely molten, providing independent evidence that H chondrite-like parent bodies could
 689 possibly be partially differentiated (Weiss & Elkins-Tanton, 2013). Secondly, the par-
 690 tially melted nature of Portales Valley supports the partial differentiation of its parent
 691 body if this meteorite was heated solely by the decay of ^{26}Al (Ruzicka et al., 2005).

692 **4.3 Implications of partially differentiated asteroids**

693 Our thermal and magnetic observations are consistent with episodic accretion of
 694 chondrules and other chondrite components to form the H chondrite parent body. Johansen
 695 et al. (2015) predict that asteroids with radii >100 km likely gained a significant por-
 696 tion of their final mass through the late-stage addition of chondrules atop an initial plan-
 697 etesimal seed. This predicted accretion scenario is extremely similar to asteroid growth
 698 mechanism adopted in this study. This predicted size range also agrees with the range
 699 we recover for the H chondrite parent body based on both the thermal evolution and the
 700 timing of the end of core solidification (Figs. 5 and 8), supporting the hypothesis that
 701 some asteroids underwent episodic accretion of chondrules.

702 We assume in our model that both accretion events are instantaneous. Although
 703 this accretion timescale is impossible and we adopted it for simplicity, the similarity in
 704 chondrule size and chemistry across different members of the same chondrite group and
 705 the estimated turbulent diffusion timescales during nebula accretion indicate that chon-
 706 dritic material accreted over short periods (<0.2 Myr; Alexander (2005)). Indeed, pre-
 707 vious modelling studies suggest the thermal evolution of bodies that formed by gradual
 708 accretion over short time periods can agree with that measured from the H chondrites
 709 (Monnereau et al., 2013). Given our results suggest that instantaneous chondrule accre-
 710 tion at times between 2.3 - 2.5 Myr after CAI formation produces acceptable fits to the
 711 measured H chondrite ages, we expect that a gradual second accretion event spanning
 712 $\sim 2.3 - 2.5$ Myr after CAI formation will introduce a similar amount of heat to the chon-
 713 dritic portion of the final body, so likely also produce acceptable fits to the measured H
 714 chondrite thermal evolutions. As our recovered range of t_2 values that produce accept-

715 able fits is close to the end of our range of possible t_1 times (0.0 - 2.0 Myr after CAI for-
 716 mation), it may be possible that one prolonged accretion event lasting from sometime
 717 <2.0 to ~ 2.5 Myr after CAI formation could also produce partially differentiated bod-
 718 ies (Lichtenberg et al., 2018) that could be consistent with the measured magnetisation
 719 and thermal evolution of the H chondrites.

720 If the accretion events in the incremental scenario supported by this study differed
 721 in time by 10^5 - 10^6 yr, it is possible that the material added to the body during each
 722 event could originate from separate chemical and isotopic reservoirs present at different
 723 times and locations in the early solar system. This accretion history challenges a cen-
 724 tral common assumption of modern meteorite classification schemes that meteorite groups
 725 are samples of distinct parent planetesimals that form from material originating from
 726 individual reservoirs (Weiss & Elkins-Tanton, 2013; Wiesberg et al., 2006). Instead, it
 727 is possible that incremental accretion could produce chondrites and achondrites that orig-
 728 inate from the same, radially-layered partially differentiated body that need not share
 729 the same genetic chemical and isotopic origin. As such, it is possible that the great di-
 730 versity of meteorite groups reflected in these classification schemes may belie underly-
 731 ing simpler genetic relationships between these groups.

732 Finally, our observations suggest that the surface of an asteroid may not be rep-
 733 resentative of its internal structure and composition. Specifically, our modelling suggests
 734 that asteroids with chondritic surfaces could have varying extents of internal melting and
 735 differentiation. The different internal structures in partially differentiated and undiffer-
 736 entiated bodies would produce different density profiles with depth throughout these bod-
 737 ies, so it may be possible to use this property to distinguish between these types of as-
 738 teroid and assess the extent of internal melting and differentiation within bodies with
 739 primitive surfaces (Weiss et al., 2012).

740 5 Conclusions

- 741 • The parent asteroids of chondrites are thought not to have partially melted through
 742 endogenic heating and undergone igneous differentiation and core formation.
- 743 • We measured the magnetic remanence carried in metal veins in the H6 ordinary
 744 chondrite Portales Valley using synchrotron X-ray microscopy. We found that nanos-
 745 tructures in these veins recorded a spatially-uniform magnetic remanence as they

746 formed during low-temperature recrystallisation over a relatively long period (tens
747 to hundreds of years) at ~ 100 Myr after CAI formation. This observation indi-
748 cates this meteorite experienced a late-stage and relatively long-lived magnetic field.

- 749 • The longevity and age of this field are inconsistent with external sources of mag-
750 netic field such as the nebula, solar wind or impacts. Instead, these properties are
751 consistent with the expected properties of fields generated by internal core dynamo
752 activity, indicating that the H chondrite parent body contained an advancing metal-
753 lic core and was, therefore, partially differentiated.
- 754 • Thermal evolution models demonstrate that incremental accretion over $10^5 - 10^6$
755 yr can result in partially differentiated bodies with thermal histories that agree
756 with the measured ages and cooling rates of multiple H chondrites. These mod-
757 els also demonstrate that such bodies can have partially molten cores at ~ 100 Myr
758 after CAI formation, so could have feasibly generated a dynamo field at the time
759 that Portales Valley recorded its remanence.
- 760 • These observations support a spectrum of internal differentiation within some as-
761 teroids with chondritic surfaces, suggest that accretion could have been a prolonged
762 process and hint that a single body could be composed of material from multiple
763 chemical and isotopic reservoirs present in the early solar system, permitting di-
764 verse meteorite groups to possibly originate from a common, radially-heterogeneous
765 parent asteroid.

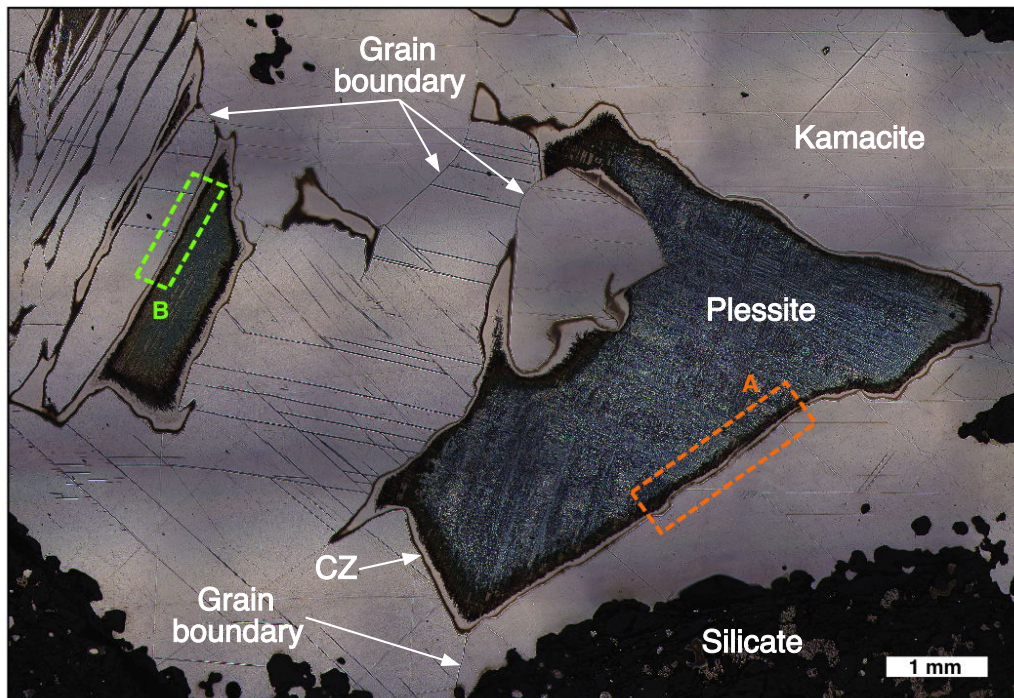


Figure 1. Optical microscopy image of the interfaces we measured in our sample of Portales Valley. The sample had been etched with 2% nital for 20 seconds prior to imaging to highlight the microstructures. The area of the cloudy zone (CZ) along interfaces A and B that we measured are labelled with coloured boxes.

Acknowledgments

We thank C. Nichols, R. Harrison and E. Lima for assistance and helpful discussions. J.A. thanks the Caltech Summer Undergraduate Research Fellowship program. J.F.J.B. and B.P.W. thank the NASA Solar System Exploration Research Virtual Institute grant #NNA14AB01A, the NASA Solar System Workings Program (grant #NNX15AL62G) and Thomas F. Peterson, Jr. for support. J.F.J.B would also like to thank St. John's College, University of Cambridge for funding. The Advanced Light Source is supported by the Director, Office of Science, Office of Basic Energy Sciences of the U.S. D.O.E. under contract #DE-AC02-05CH11231. We would like to thank the Natural History Museum, London and the U.S. National Museum for loaning us meteorites. The data in this paper can be found on the MagIC database (<https://www2.earthref.org/MagIC>).

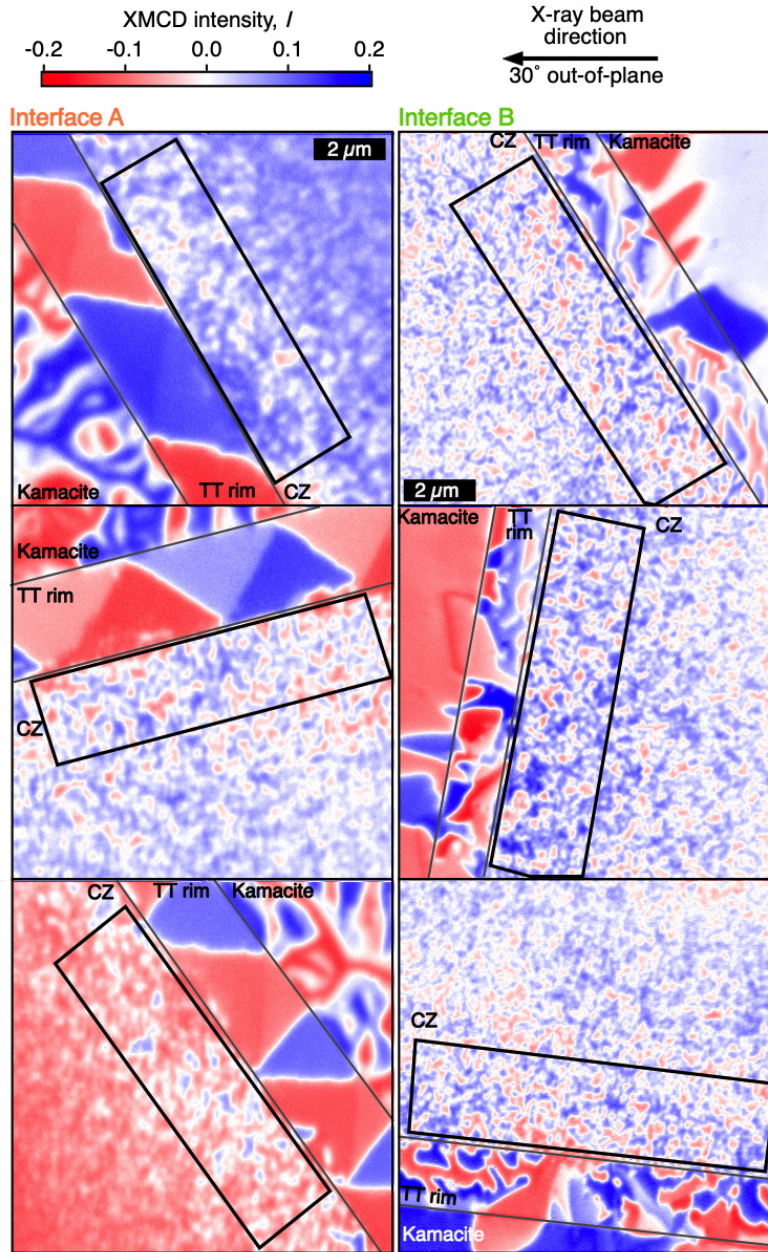


Figure 2. XPEEM images of the CZ in our sample of Portales Valley. These images are representative of the images we captured along interface A (left panels) and B (right panels). Images were acquired at three sample rotations (top, middle, and bottom rows). The colour depicts the XMCD intensity, with blue and red signals corresponding to positive and negative projections along the X-ray beam direction (top right, constant across all panels), respectively. The paleofield properties were calculated from the average XMCD intensity extracted from the regions within the black boxes in each panel. The scale bars for all images from interface A and B are included in the top panel for each interface. The kamacite, tetraenaite (TT) rim and cloudy zone (CZ) are separated by grey lines.

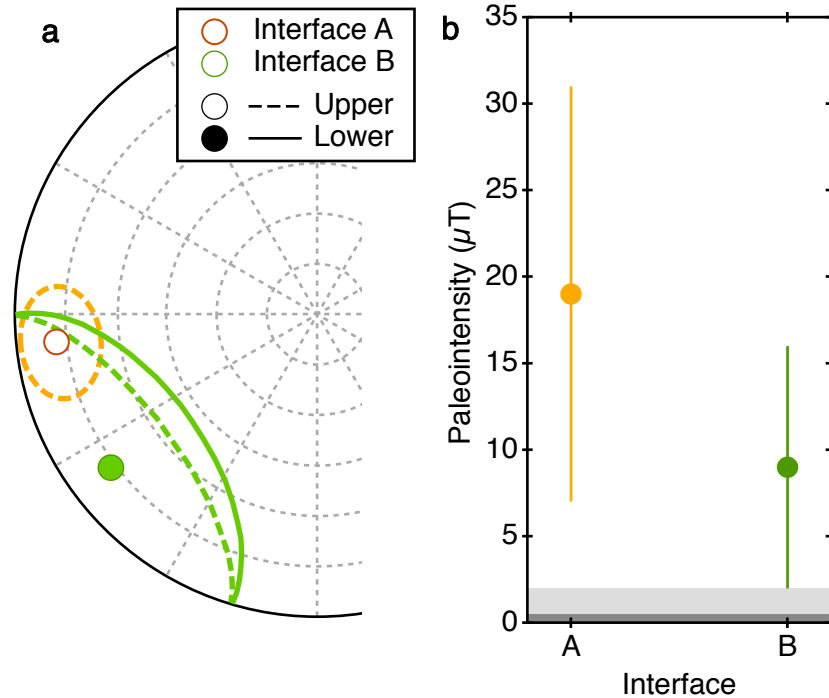


Figure 3. Ancient field properties recovered from XPEEM images of Portales Valley. **a** Stereographic projection showing the orientations of the average paleofield recovered from both interfaces studied. The 95% confidence interval along each interface calculated from the scatter in the recovered paleodirections from the different locations along each interface are included as the ellipses. Filled points and solid lines represent the lower hemisphere of the stereoplot and open points and dashed lines represent the upper hemisphere. **b** Lower limits on the paleointensities recovered from both interfaces. The total 95% uncertainties are depicted by the error bars (see Section 4.1). The calculated 95% confidence limits on the possible paleointensities that could be recovered from the absence of an applied field taken from Fig. 3 are included as a dark grey bar for 47,000 islands with a radius of 42 nm and a light grey bar for 190,000 islands with a radius of 21 nm. Our recovered paleointensities are outside of these ranges, indicating that the remanence we measure in Portales Valley is unlikely to correspond to the absence of a field.

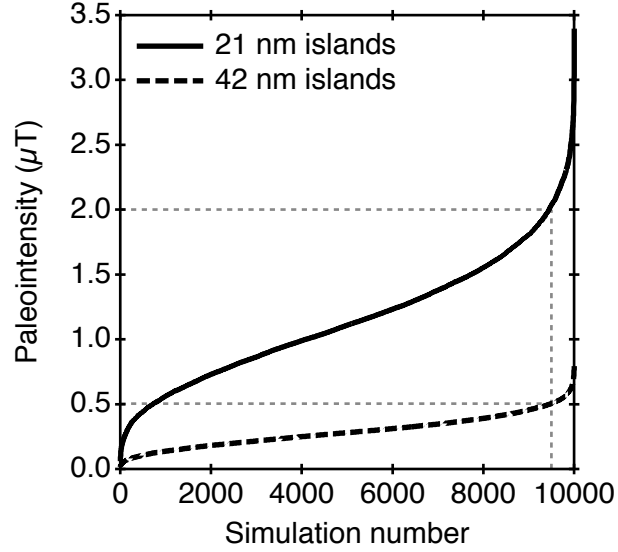


Figure 4. Cumulative probability distribution showing the paleointensities of 10,000 simulated CZs with equal probability that its islands adopt any one of the six possible magnetisation directions, corresponding to the magnetic configuration expected in the absence of an external magnetic field (see Bryson et al. (2017)). We conducted simulations with 47,000 islands with radii of 42 nm and 190,000 islands with radii of 21 nm, encompassing the possible range of island sizes and numbers we analysed. The vertical dashed lines marks 95% of the simulations, suggesting that recovered paleointensities $>0.5 \mu\text{T}$ and $>2 \mu\text{T}$ for islands with radii of 42 nm and 21 nm, respectively, are inconsistent with zero field magnetisation at the 95% confidence level.

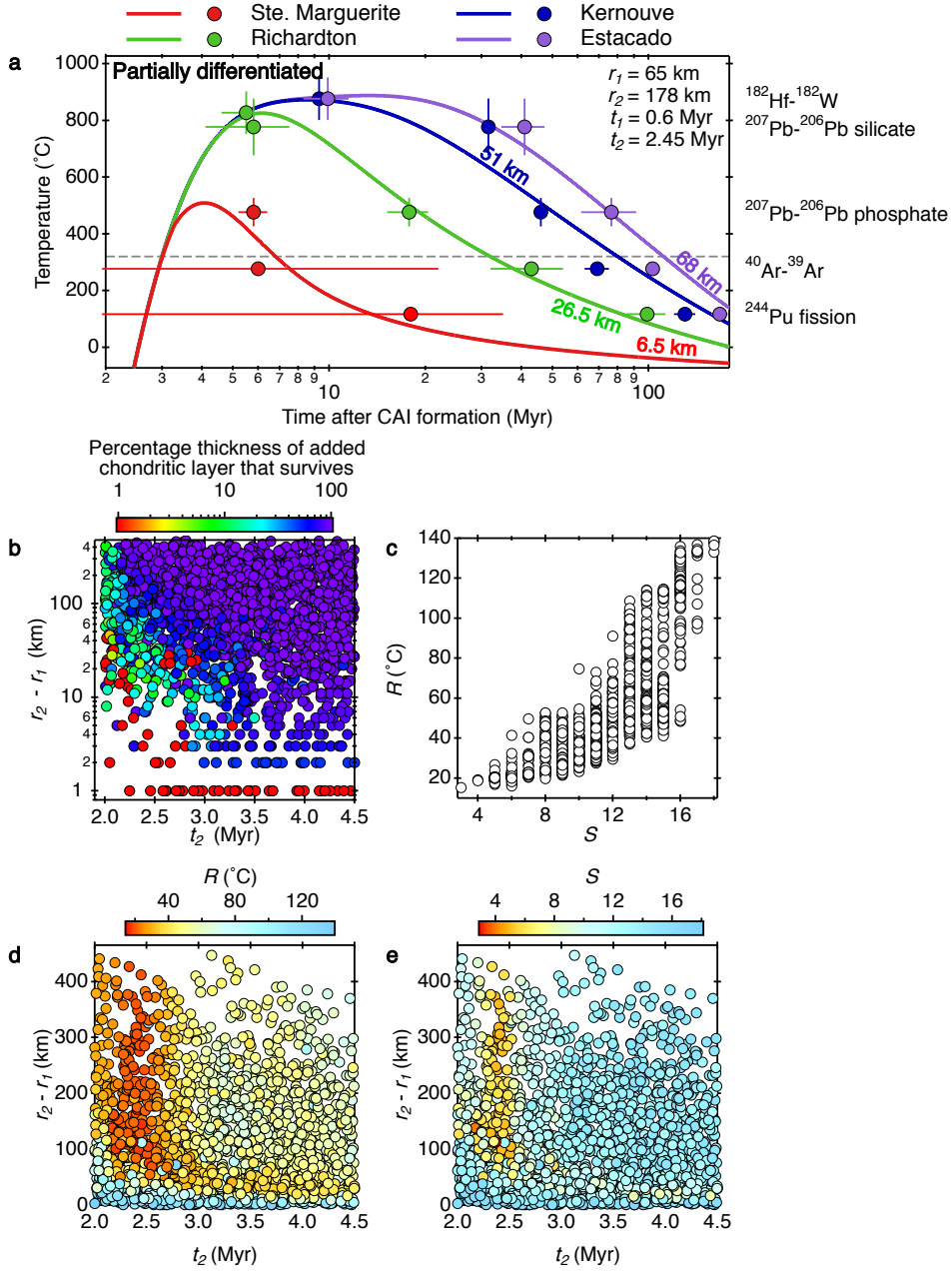


Figure 5. Thermal modelling of a partially differentiated H chondrite planetesimal. **a** Measured ages for four well-dated H chondrites (points) and modelled thermal evolutions (solid lines) for a body with parameters that produced the lowest R value in this model ($r_1 = 65 \text{ km}$, $r_2 = 178 \text{ km}$, $t_1 = 0.6 \text{ Myr}$ after CAI formation and $t_2 = 2.45 \text{ Myr}$ after CAI formation). The depth of each of the modelled thermal evolutions is included next to each curve. The parameters in this model produce $S = 5$ and an average total residual value of $R = 14.5 \text{ }^{\circ}\text{C}$. The geochronological systems are listed on the right of the figure. The horizontal dashed line depicts the tetraenaite ordering temperature. **b** All combinations of $r_2 - r_1$ and t_2 showing the proportion of the added chondritic layer that survives metamorphism without melting. **c** Plot of the two fit quality metrics. 95% of models with $S \leq 6$ have $R \leq 27 \text{ }^{\circ}\text{C}$. **d** All combinations of $r_2 - r_1$ and t_2 colour-coded by their R value. **e** All combinations of $r_2 - r_1$ and t_2 colour-coded by their S value. Lower values of R and S correspond to better fits.

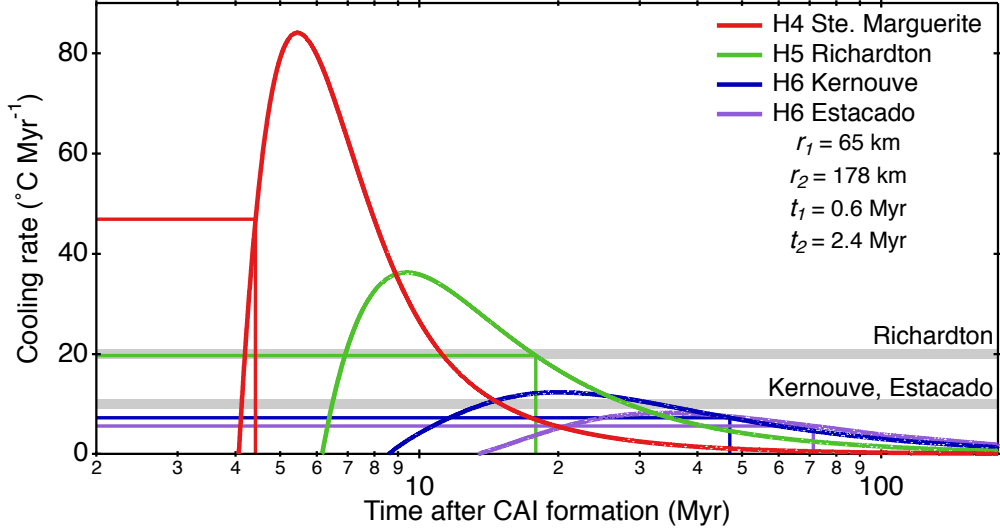


Figure 6. Calculated cooling rate evolution from the curves in Fig. 4a. Measured metallographic cooling rates correspond to the cooling rate of a meteorite as it cooled through ~ 500 $^{\circ}\text{C}$ and are depicted by horizontal grey bars (Scott et al., 2014). The time that each meteorite reached this temperature is depicted by the coloured vertical lines. The corresponding cooling rate at this time is depicted by the coloured horizontal lines. In our model, the peak metamorphic temperature of Ste. Marguerite only just exceeded 500 $^{\circ}\text{C}$, so this depth cooled through 500 $^{\circ}\text{C}$ while its cooling rate was still increasing. The experimental cooling rate of Ste. Marguerite is $\sim 10,000$ $^{\circ}\text{C}/\text{Myr}$, which is far faster than any cooling rate achieved in our models, so is likely due to a non-ideal effect not included in our models (e.g., an impact).

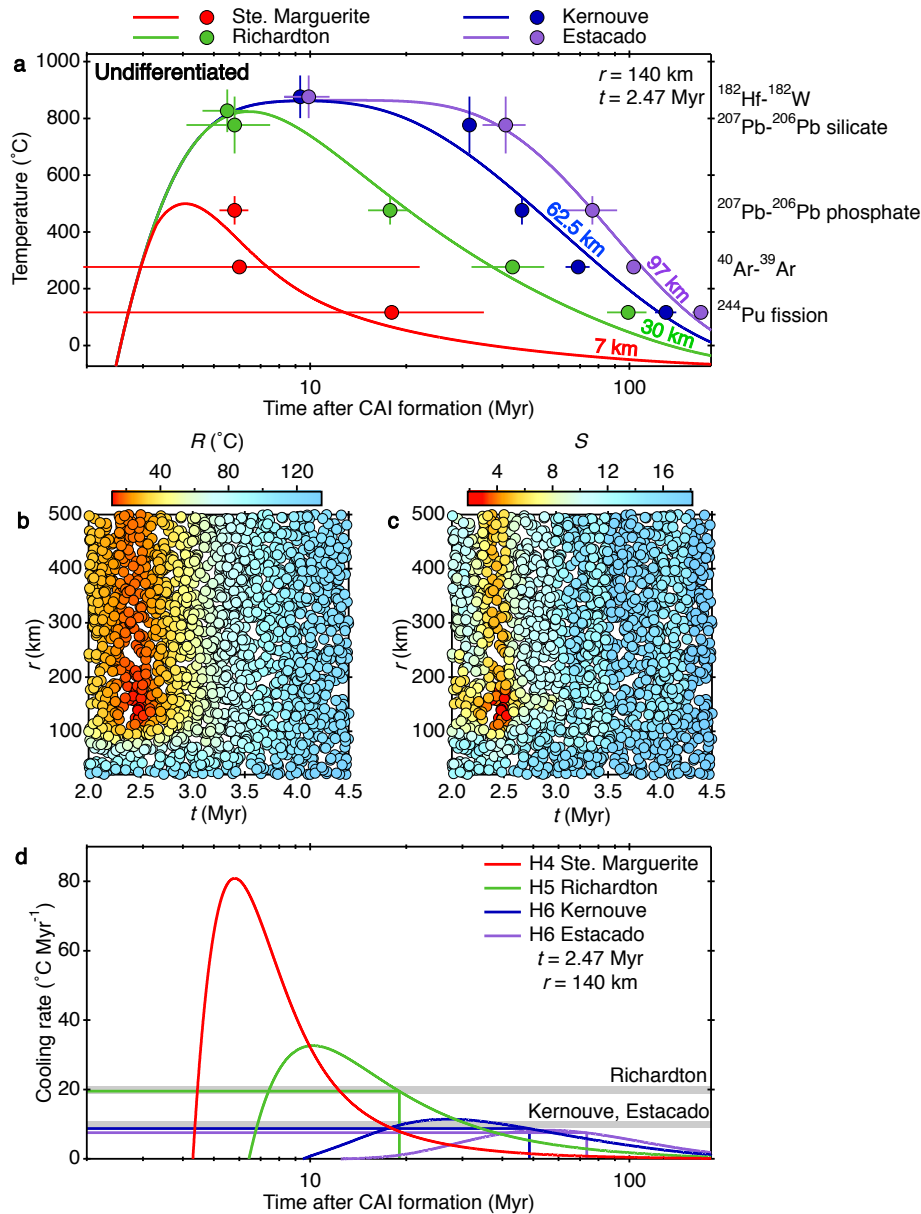


Figure 7. Thermal modelling of an undifferentiated H chondrite planetesimal. **a** Measured ages for four well-dated H chondrites (points) and modelled thermal evolutions (solid lines) for a body with parameters that produced the lowest R value in this model ($r = 140 \text{ km}$ and $t = 2.47 \text{ Myr}$ after CAI formation). The depth of each of the modelled thermal evolutions is included next to each curve. The parameters in this model produce an average total residual value of $R = 12.7 \text{ }^{\circ}\text{C}$ and $S = 2$. The geochronological systems are listed on the right of the figure. **b** All combinations of r and t colour-coded by the R value of the simulation. **c** All combinations of r and t colour-coded by the S value of the simulation. **d** Calculated cooling rate evolution from the curves in **a**. Measured metallographic cooling rates correspond to the cooling rate of a meteorite as it cooled through $\sim 500 \text{ }^{\circ}\text{C}$ and are depicted by horizontal grey bars (Scott et al., 2014). The time that each meteorite reached this temperature is depicted by the coloured vertical lines. The corresponding cooling rate at this time is depicted by the coloured horizontal lines. The recovered depth of Ste. Marguerite in this model did not reach $500 \text{ }^{\circ}\text{C}$.

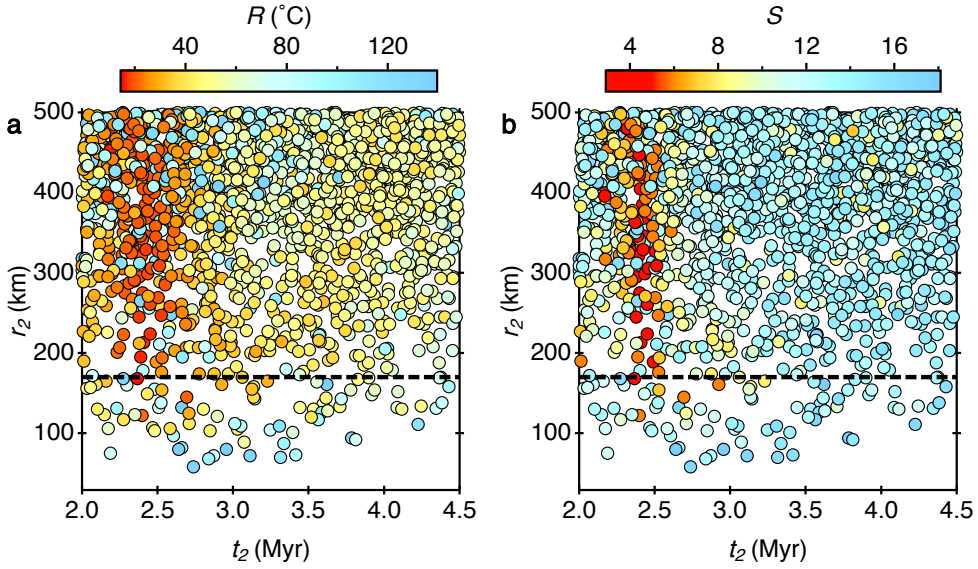


Figure 8. All combinations of r_2 and t_2 from our partially differentiated model colour-coded by **a** R and **b** S values of the simulation. The dashed black line depicts $r_2 = 170$ km, which represents the critical radius above which bodies can have at least partially liquid cores at 100 Myr after CAI formation, so could feasibly have been generating a magnetic field at the time that Portales Valley recorded its remanence (Bryson et al., 2019). A wide range of r_2 values >170 km produce acceptable fits.

777 **References**

- 778 Alexander, C. M. O. (2005). From supernovae to planets: The view from mete-
 779 orites and interplanetary dust particles. In A. N. Krot, E. R. D. Scott, &
 780 B. Reipurth (Eds.), *Chondrites and the protoplanetary disk* (Vol. 341, pp.
 781 972–1002).
- 782 Amelin, Y., Ghosh, A., & Rotenberg, E. (2005). Unraveling the evolution of chon-
 783 drite parent asteroids by precise U-Pb dating and thermal modeling. *Geochim-*
 784 *ica et Cosmochimica Acta*, *69*, 505–518.
- 785 Berndt, T., Muxworthy, A. R., & Fabian, K. (2016). Does size matter? Statistical
 786 limits of paleomagnetic field reconstruction from small rock specimens. *Journal*
 787 *of Geophysical Research: Solid Earth*, *121*, 15–26.
- 788 Blackburn, T., Alexander, C. M. O., Carlson, R., & Elkins-Tanton, L. T. (2017).
 789 The accretion and impact history of the ordinary chondrite parent bodies.
 790 *Geochimica et Cosmochimica Acta*, *200*, 201–217.
- 791 Blinova, A., Amelin, Y., & Samson, C. (2007). Constraints on the cooling history of
 792 the H-chondrite parent body from phosphate and chondrule Pb-isotopic dates
 793 from Estacado. *Meteoritics and Planetary Science*, *42*, 1337–1350.
- 794 Bogard, D. D., & Garrison, D. H. (2009). Ar–Ar and I–Xe ages and thermal histo-
 795 ries of three unusual metal-rich meteorites. *Geochimica et Cosmochimica Acta*,
 796 *73*, 6965–6983.
- 797 Bouvier, A., Blichert-Toft, J., Moynier, F., Vervoort, J. D., & Albarede, F. (2007).
 798 Pb–Pb dating constraints on the accretion and cooling history of chondrites.
 799 *Geochimica et Cosmochimica Acta*, *71*, 1583–1604.
- 800 Bryson, J. F. J., Church, N. S., Kasama, T., & Harrison, R. J. (2014). Nanomag-
 801 netic intergrowths in Fe–Ni meteoritic metal: The potential for time-resolved
 802 records of planetesimal dynamo fields. *Earth and Planetary Science Letters*,
 803 *388*, 237–248.
- 804 Bryson, J. F. J., Herrero-Albillos, J., Kronast, F., Ghidini, M., Redfern, S. A. T.,
 805 van der Laan, G., & Harrison, R. J. (2014). Nanopaleomagnetism of mete-
 806 oritic Fe–Ni studied using X-ray photoemission electron microscopy. *Earth and*
 807 *Planetary Science Letters*, *396*, 125–133.
- 808 Bryson, J. F. J., Neufeld, J. A., & Nimmo, F. (2019). Constraints on asteroid
 809 magnetic field evolution and the radii of meteorite parent bodies from thermal

- 810 modelling. *Earth and Planetary Science Letters*.
- 811 Bryson, J. F. J., Nichols, C. I. O., Herrero-Albillos, J., Kronast, F., Kasama, T.,
812 Alimadadi, H., ... Harrison, R. J. (2015). Long-lived magnetism from
813 solidification-driven convection on the pallasite parent body. *Nature*, *517*,
814 472–475.
- 815 Bryson, J. F. J., Weiss, B. P., Harrison, R. J., Herrero-Albillos, J., & Kronast, F.
816 (2017). Paleomagnetic evidence for dynamo activity driven by inward crys-
817 tallisation of a metallic asteroid. *Earth and Planetary Science Letters*, *472*,
818 152–163.
- 819 Carporzen, L., Weiss, B. P., Elkins-Tanton, L. T., Shuster, D. L., Ebel, D. S., &
820 Gattacceca, J. (2011). Magnetic evidence for a partially differentiated carbona-
821 ceous chondrite parent body. *Proceedings of the National Academy of Sciences*,
822 *108*, 6386–6389.
- 823 Cisowski, S. M. (1987). Magnetism of meteorites. , *2*, 525–560.
- 824 Crawford, D., & Schultz, P. (2000). Electrostatically charged impact ejecta and im-
825 plications for lunar paleomagnetism,. *Lunar and Planetary Science Conference*
826 *XXXI*, Abstract 1849.
- 827 Dos Santos, E., Gattacceca, J., Rochette, P., Fillion, G., & Scorzelli, R. B. (2015).
828 Kinetics of tetrataenite disordering. *Journal of Magnetism and Magnetic Mate-*
829 *rials*, *375*, 234–241.
- 830 Doyle, P. M., Jogo, K., Nagashima, K., Krot, A. N., Wakita, S., Ciesla, F. J., &
831 Hutcheon, I. D. (2015). Early aqueous activity on the ordinary and carbona-
832 ceous chondrite parent bodies recorded by fayalite. *Nature Communications*,
833 *6*, 7444.
- 834 Einsle, J. F., Eggeman, A. S., Martineau, B. H., Saghi, Z., Collins, S. M., Blukis, R.,
835 ... Harrison, R. J. (2018). Nanomagnetic properties of the meteorite cloudy
836 zone. *Proceedings of the National Academy of Sciences*, *115*, E11436–E11445.
- 837 Elkins-Tanton, L. T., Weiss, B. P., & Zuber, M. T. (2011). Chondrites as samples of
838 differentiated planetesimals. *Earth and Planetary Science Letters*, *305*, 1–10.
- 839 Fu, R. R., Lima, E. A., & Weiss, B. P. (2014). No nebular magnetization in the Al-
840 lende CV carbonaceous chondrite. *Earth and Planetary Science Letters*, *404*,
841 54–66.
- 842 Fu, R. R., Weiss, B. P., Shuster, D. L., Gattacceca, J., Grove, T. L., Suavet, C., ...

- 843 Kuan, A. T. (2012). An ancient core dynamo in asteroid Vesta. *Science*, *338*,
844 238–241.
- 845 Gattacceca, J., & Rochette, P. (2004). Toward a robust normalized magnetic paleo-
846 ointensity method applied to meteorites. *Earth and Planetary Science Letters*,
847 *227*, 377–393.
- 848 Gattacceca, J., Suavet, C., Rochette, P., Weiss, B. P., Winklhofer, M., Uehara, M.,
849 & Friedrich, J. M. (2014). Metal phases in ordinary chondrites: Magnetic
850 hysteresis properties and implications for thermal history. *Meteoritics and*
851 *Planetary Science*, *49*, 652–676.
- 852 Gattacceca, J., Weiss, B. P., & Gounelle, M. (2016). New constraints on the mag-
853 netic history of the CV parent body and the solar nebula from the Kaba
854 meteorite. *Earth and Planetary Science Letters*, *455*, 166–175.
- 855 Goldstein, J. I., Scott, E. R. D., & Chabot, N. L. (2009). Iron meteorites: Crys-
856 tallization, thermal history, parent bodies, and origin. *Chemie der Erde - Geo-*
857 *chemistry*, *69*, 293–325.
- 858 Henke, S., Gail, H. P., Tieloff, M., & Schwartz, W. H. (2013). Thermal evolution
859 model for the H chondrite asteroid - instantaneous formation versus protracted
860 accretion. *Icarus*, *226*, 212–228.
- 861 Hevey, P. J., & Sanders, I. S. (2006). A model for planetesimal meltdown by ^{26}Al
862 and its implications for meteorite parent bodies. *Meteoritics and Planetary*
863 *Science*, *41*, 95–106.
- 864 Johansen, A., Low, M. M., Lacerda, P., & Bizzarro, M. (2015). Growth of aster-
865 oids, planetary embryos, and Kuiper belt objects by chondrule accretion. *Sci-*
866 *ence Advances*, *17*, e1500109.
- 867 Kirschvink, J. L. (1980). The least-squares line and plane and the analysis of paleo-
868 magnetic data. *Geophysical Journal International*, *62*, 699–718.
- 869 Kirschvink, J. L., Kopp, R. E., Raub, T. D., Baumgartner, C. T., & Holt, J. W.
870 (2008). Rapid, precise, and high-sensitivity acquisition of paleomagnetic and
871 rock-magnetic data: Development of a low-noise automatic sample changing
872 system for superconducting rock magnetometers. *Geochemistry, Geophysics,*
873 *Geosystems*, *9*, Q05Y01.
- 874 Kleine, T., Touboul, M., van Orman, J. A., Bourdon, B., Maden, C., Mezger, K.,
875 & Halliday, A. N. (2008). Hf–W thermochronometry: Closure temperature

- 876 and constraints on the accretion and cooling history of the H chondrite parent
877 body. *Earth and Planetary Science Letters*, *270*, 106–118.
- 878 Lichtenberg, T., Golabek, G. J., Dullemond, C. P., Schönbächler, M., Gerya, T. V.,
879 & Meyer, M. R. (2018). Impact splash chondrule formation during planetesi-
880 mal recycling. *Icarus*, *302*, 27–43.
- 881 Maurel, C., Bryson, J. F. J., Weiss, B. P., & Scholl, A. (2018). Paleomagnetic ev-
882 idence for a layered partially differentiated iron–meteorite parent body. *Lunar
883 and Planetary Science Conference XLIX, Abstract 1171*.
- 884 Maurel, C., Weiss, B. P., & Bryson, J. F. J. (2019). Meteorite cloudy zone formation
885 as a quantitative indicator of paleomagnetic field intensities and cooling rates
886 on planetesimals. *Earth and Planetary Science Letters*, *513*, 166–175.
- 887 Monnereau, M., Toplis, M. J., Baratoux, C., & Guignard, J. (2013). Thermal history
888 of the H-chondrite parent body: Implications for the metamorphic grade and
889 accretionary time–scales. *Geochimica et Cosmochimica Acta*, *119*, 302–321.
- 890 Morris, D. G., Besag, F. M. C., & Smallman, R. E. (1974). Ordering and disordering
891 in Cu_3Au . *The Philosophical Magazine: A Journal of Theoretical Experimental
892 and Applied Physics*, *29*, 43–57.
- 893 Muxworthy, A. R., Bland, P. A., Davison, T. M., Moore, J., Collins, G. S., & Ciesla,
894 F. J. (2017). Evidence for an impact–induced magnetic fabric in Allende, and
895 exogenous alternatives to the core dynamo theory for Allende magnetization.
896 *Meteoritics and Planetary Science*, *52*, 2132–2146. doi: 10.1111/maps.12918
- 897 Néel, L., Pauleve, J., Pauthenet, R., Laugier, J., & Dautreppe, D. (1964). Magnetic
898 properties of an Iron-Nickel single crystal ordered by neutron bombardment.
899 *Journal of Applied Physics*, *35*, 873–876.
- 900 Neufeld, J. A., Bryson, J. F. J., & Nimmo, F. (2019). The top–down solidification
901 of iron asteroids driving dynamo evolution. *Journal of Geophysical Research:
902 Planets*.
- 903 Nichols, C. I. O., Bryson, J. F. J., Herrero-Albillos, J., Kronast, F., Nimmo, F.,
904 & Harrison, R. J. (2016). Pallasite paleomagnetism: Quiescence of a core
905 dynamo. *Earth and Planetary Science Letters*, *441*, 103–112.
- 906 Nichols, C. I. O., Krakow, R., Herrero-Albillos, J., Kronast, F., Northwood-Smith,
907 G., & Harrison, R. J. (2018). Microstructural and paleomagnetic insight into
908 the cooling history of the IAB parent body. *Geochimica et Cosmochimica*

- 909 *Acta*, 229, 1–19.
- 910 Nimmo, F. (2009). Energetics of asteroid dynamos and the role of compositional
911 convection. *Geophysical Research Letters*, 36, L10210.
- 912 Opeil, C. P., Consolmagno, G. J., Safarik, D. J., & Britt, D. T. (2012). Stony me-
913 teorite thermal properties and their relationship with meteorite chemical and
914 physical states. *Meteoritics and Planetary Science*, 47, 319–329.
- 915 Oran, R., Weiss, B. P., & Cohen, O. (2018). Were chondrites magnetized by the
916 early solar wind? *Earth and Planetary Science Letters*, 492, 222–231.
- 917 Rochette, P., Gattacceca, J., Bonal, L., Bourot-Denise, M., Chevier, V., Clerc, J. P.,
918 ... Skripnik, A. (2008). Magnetic classification of stony meteorites: 2. Non-
919 ordinary chondrites. *Meteoritics and Planetary Science*, 43, 959–980.
- 920 Rochette, P., Sagnotti, L., Bourot-Denise, M., Consolmagno, G., Folco, L., Gattac-
921 ceca, J., ... Pesonen, L. (2003). Magnetic classification of stony meteorites: 1.
922 Ordinary chondrites. *Meteoritics and Planetary Science*, 38(2), 251–268.
- 923 Rubin, A. E. (2004). Postshock annealing and postannealing shock in equilibrated
924 ordinary chondrites: implications for the thermal and shock histories of chon-
925 dritic asteroids. *Geochimica et Cosmochimica Acta*, 68, 673–689.
- 926 Ruckriemen, T., Breuer, D., & Spohn, T. (2015). The Fe snow regime in
927 Ganymede’s core: A deep-seated dynamo below a stable snow zone. *Jour-
928 nal of Geophysical Research: Planets*, 120, 1095–1118.
- 929 Ruzicka, A., Hugo, R., & Hutson, M. (2015). Deformation and thermal histories
930 of ordinary chondrites: Evidence for post-deformation annealing and syn-
931 metamorphic shock. *Geochimica et Cosmochimica Acta*, 163, 219–233.
- 932 Ruzicka, A., Killgore, M., Mittlefehldt, D. W., & Fries, M. D. (2005). Portales Val-
933 ley: Petrology of a metallic-melt meteorite breccia. *Meteoritics and Planetary
934 Science*, 40, 261–295.
- 935 Scott, E. R. D., Krot, T. V., Goldstein, J. I., & Wakita, S. (2014). Thermal and
936 impact history of the H chondrite parent asteroid during metamorphism: Con-
937 straints from metallic Fe–Ni. *Geochimica et Cosmochimica Acta*, 136, 13–37.
- 938 Shah, J., Bates, H. C., Muxworthy, A. R., Hezel, D. C., Russell, S. S., & Genge,
939 M. J. (2017). Long-lived magnetism on chondrite parent bodies. *Earth and
940 Planetary Science Letters*, 475, 106–118.
- 941 Stephenson, A. (1993). Three-axis static alternating field demagnetization of rocks

- 942 and the identification of natural remanent magnetization, gyroremanent mag-
 943 netization, and anisotropy. *Journal of Geophysical Research*, *98*, 373–381.
- 944 Stöffler, D., Keil, K., & Scott, E. R. D. (1991). Shock metamorphism of ordinary
 945 chondrites. *Geochimica et Cosmochimica Acta*, *55*, 3845–3867.
- 946 Tarduno, J. A., O’Brien, T. M., Blackman, E. G., & Smirnov, A. V. (2017). Magne-
 947 tization of CV meteorites in the absence of a parent body core dynamo. *Lunar
 948 and Planetary Science Conference XLVIII, Abstract 2850*.
- 949 Tauxe, L., & Staudigel, H. (2004). Strength of the geomagnetic field in the Cre-
 950 taceous Normal Superchron: New data from submarine basaltic glass of the
 951 Troodos Ophiolite. *Geochemistry, Geophysics, Geosystems*, *5*, Q02H06.
- 952 Tikoo, S. M., Gattacceca, J., Swanson-Hysell, N. L., & Weiss, B. P. (2015). Preser-
 953 vation and detectability of shock-induced magnetization. *Journal of Geophysi-
 954 cal Research: Planets*, *120*, 1461–1475.
- 955 Trieloff, M., Jessberger, E. K., Herrwerth, I., Hopp, J., Fieni, C., Ghelis, M., ...
 956 Pellas, P. (2003). Structure and thermal history of the H-chondrite parent
 957 asteroid revealed by thermochronometry. *Nature*, *422*, 502–506.
- 958 Uehara, M., Gattacceca, J., Leroux, H., Jacob, D., & van der Beek, C. J. (2011).
 959 Magnetic microstructures of metal grains in equilibrated ordinary chondrites
 960 and implications for paleomagnetism of meteorites. *Earth and Planetary Sci-
 961 ence Letters*, *306*, 241–252.
- 962 Wang, H., Weiss, B. P., Bai, X.-N., Downey, B. G., Wang, J., Wang, J., ... Zu-
 963 colotto, M. E. (2017). Lifetime of the solar nebula constrained by meteorite
 964 paleomagnetism. *Science*, *355*, 623–627.
- 965 Warren, P. H. (2011). Ejecta-megaregolith accumulation on planetesimals and large
 966 asteroids. *Meteoritics and Planetary Science*, *46*, 53–78.
- 967 Weiss, B. P., & Elkins-Tanton, L. T. (2013). Differentiated planetesimals and the
 968 parent bodies of chondrites. *Annual Review of Earth and Planetary Sciences*,
 969 *41*, 529–560.
- 970 Weiss, B. P., Elkins-Tanton, L. T., Barucci, M. A., Sierks, H., Snodgrass, C., Vin-
 971 cent, J.-B., ... Schulz, R. (2012). Possible evidence for partial differentiation
 972 of asteroid Lutetia from Rosetta. *Planetary and Space Science*, *66*, 137–146.
- 973 Weiss, B. P., Gattacceca, J., Stanley, S., Rochette, P., & Christensen, U. R. (2010).
 974 Paleomagnetic records of meteorites and early planetesimal differentiation.

975 *Space Science Reviews*, 152, 341–390.

976 Weiss, B. P., & Tikoo, S. M. (2014). The lunar dynamo. *Science*, 346, 1246753.

977 Wiesberg, M. K., McCoy, T. J., & Krot, A. N. (2006). Systematics and evaluation of
978 meteorite classification. , 19–52.

979 Williams, Q. (2009). Bottom–up versus top–down solidification of the cores of small
980 solar system bodies: Constraints on paradoxical cores. *Earth and Planetary
981 Science Letters*, 284, 564–569.